MULTIPLE-DOMAIN ANALYSIS OF 3-DIMENSIONAL FLOW OVER AN ELLIPSOIDAL BODY OF AERONAUTICAL INTEREST

by

Erkan Sevinç

B.Sc., Aeronautics Engineering, Istanbul Technical University, 1995

Submitted to the

Institute for Graduate Studies in Science and Engineering

in partial fulfillment of the requirements for the degree of

Master of Science

Graduate Program in Mechanical Engineering

Boğaziçi University

2006

MULTIPLE-DOMAIN ANALYSIS OF 3-DIMENSIONAL FLOW OVER AN ELLIPSOIDAL BODY OF AERONAUTICAL INTEREST

APPROVED BY:

Assist. Prof. Ali Ecder (Thesis Supervisor)	. . . . .
Assist. Prof. Kunt Atalık	. . . . .
Assoc. Prof. Can Özturan	. . . . .

DATE OF APPROVAL: 11.09.2006

to the memory of my beloved father, Mehmet SEVİNÇ

ACKNOWLEDGEMENTS

I would like to thank to my advisor Dr. Ali Ecder who encouraged me to complete this study. I would also like to thank to my wife Senem and my little daughter Selin for their patience during my study and my friends who supported me every time I needed. Finally, thanks to the friends at our CFD laboratory.

ABSTRACT

MULTIPLE-DOMAIN ANALYSIS OF 3-DIMENSIONAL FLOW OVER AN ELLIPSOIDAL BODY OF AERONAUTICAL INTEREST

Numerical solutions to partial differential equations form the backbone of mathematical models that simulate gas flow, which in the present case is assumed to be airflow around an arbitrary atmospheric body. Significance of simulating airflow in three dimensions reveals itself with the developing aviation industry and increasing needs for obtaining accurate results during the design process of atmospheric vehicles.

A three dimensional approach is deemed necessary for accuracy reasons and the opportunity to compare results with that of 2-D flow assumptions. As the number of nodes in the computational domain increases by a factor of the number of nodes in one dimension, excessive computational work is expected. As such, performance of the numerical solution algorithm gains importance more than anything in the whole burden. Adapting a multi-grid algorithm is hence expected to be a wise step towards solution. The effects of leveling in the multi grid domain are of primary interest.

The primary objective of this study is to develop computational tools that facilitate and speed up the solution of three-dimensional external flows around non-symmetric bodies. Adapting multiple domains in the computational space is a sort of domain decomposition technique. Overlapping domains where each domain of coarser mesh encloses that of the finer meshes have been employed. This provided a multi-grid/multi-level formulation which resulted in faster convergence by way of reducing smooth errors. This formulation comprises constant-size sub-problems which might also exhibit good applicability in parallel computation. The effects and the advantages of multi-domains applied for finite difference formulations in three spatial coordinates were numerically experimented. Faster convergence of numerical algorithm using a multi level approach in three dimensions was achieved.

ÖZET

HAVACILIK İLE İLGİLİ ELLIPSOIDAL BİR YAPI ETRAFINDAKİ 3-BOYUTLU AKIŞIN ÇOKLU ALAN ANALİZİ

Kısmi diferansiyel denklemlerin sayısal çözümleri, mevcut çalışmada herhangi bir atmosferik cismin etrafındaki akış olarak ifade edilebilecek gaz akışlarının simüle edildiği matematik modellerin temelini oluşturmaktadır. Hava akışının üç boyutta simüle edilmesinin önemi, havacılığın gelişmesi ve atmosferik vasıtaların tasarım çalışmaları sırasında hassas çözümler elde etmek için artan ihtiyaçlar ile kendini ortaya koymuştur.

Hassasiyet ihtiyaçları ve iki boyutlu çözüm varsayımları ile elde edilen çözümler ile karşılaştırma yapabilme imkanı sebebiyle üç boyutlu akış yaklaşımı ihtiyaç görülmüştür. Hesap alanı içerisinde toplam düğüm sayısı, bir eksendeki düğüm noktası katı kadar arttığı için aşırı hesaplama işi beklenmektedir. Bu sebeple, sayısal çözüm algoritmasının performansı yapılan tüm çalışma içerisinde her şeyden daha fazla önem kazanmaktadır. Bir çoklu-alan algoritmasının uygulanması çözüme ulaşmak için akıllı bir adım olarak kabul edilebilir. Çoklu alan içerisindeki seviyelendirmenin etkileri öncelikli olarak ilgi toplamaktadır.

Bu çalışmanın birincil amacı, simetrik olmayan cisimler etrafındaki 3 boyutlu harici akışın çözümünü kolaylaştıracak ve hızlandıracak sayısal uygulamalar geliştirilmesidir. Hesap alanı içerisinde çoklu alan uygulanması bir tür alan parçalama tekniğidir. Daha seyrek olan her bir ağın daha sıkı olan diğer ağların üstüne bindiği üst-üste alanlar kullanılmıştır. Bu ise, küçük hataların azaltılması suretiyle daha hızlı yakınsama sağlayan çoklu-alan/çoklu-seviye formülasyonu temin etmiştir. Bu formülasyon, paralel hesaplama çalışmalarında da gayet iyi bir uygulama gösterebilecek olan sabit boyutlu alt problemler ihtiva etmektedir. Üç boyutlu uzayda sonlu fark formülasyonlarına uygulanan çoklu alanların etki ve avantajları sayısal olarak araştırılmıştır. Çoklu seviyelendirme yaklaşımı üç boyutta gerçekleştirilerek sayısal algoritmanın daha hızlı yakınsaması sağlanmıştır.

TABLE OF CONTENTS

ACKNOWLEDGEMENTS ..... *iv*
ABSTRACT ..... *v*
ÖZET ..... *vi*
LIST OF FIGURES ..... *viii*
LIST OF TABLES ..... *x*i
LIST OF SYMBOLS / ABBREVIATIONS ..... *xii*
1. INTRODUCTION 1
2. MATHEMATICAL MODELING IN SPHERICAL POLAR COORDINATE SYSTEM 4
2.1 The Alternating Direction Implicit (ADI) Method 5
2.2 Gauss Seidel Iteration Scheme 9
3. MATHEMATICAL MODELING IN OBLATE SPHEROIDAL COORDINATE SYSTEM 12
4. COMPUTATIONAL RESULTS 16
4.1 Solution of the Potential Function in 3-D Spherical Polar Coordinates 16
4.2 Solution of the Potential Function In 3-D Oblate Spheroidal Coordinates 20
4.2.1. Effects of the Selection of Oblate Spheroidal Coordinate System in the Solution Field 26
4.2.2 Adaptation of Multi-Domain Approach 29
4.2.3 Effects In Response to Adaptation of Multi Domain Approach 34
4.3 Solution of 3-D Potential Flow 37
4.3.1. How to Model a Potential Flow 38
4.3.2. Velocity Components in Oblate Spheroidal Coordinates and Back Transformation into Physical Space 42
4.3.3 Flow Field 45
5. CONCLUSIONS 52
REFERENCES 54

LIST OF FIGURES

Figure 4.1	Cross sectional view of the spherical domain ……	17
Figure 4.2	Perspective view of the cross sectional mesh of Fig. 4.1 ……..	17
Figure 4.3	Graphical representation of the solution for 3-D temperature field …	18
Figure 4.4	Perspective view of the graphical representation of Fig. 4.3 …….	19
Figure 4.5	A graphical representation of a cross volume ……	20
Figure 4.6	Cross sectional view of 3-D domain comprising the 3-D ellipsoidal body……	21
Figure 4.7	Perspective view of the cross sectional mesh of Fig. 4.6 ……	22
Figure 4.8	Cross sectional zoom on the center of the mesh …….	22
Figure 4.9a-b	Graphical representations of the solution field for 3-D temperature field, at central x-axis and y-axis ……	23
Figure 4.9c	Graphical representations of the solution field for 3-D temperature field, at central z-axis……...	24
Figure 4.10	The 3-D ellipsoid around which the solution to the potential function is sought …….	24
Figure 4.11	Cross sectional view of the solution field at y=0 (side view, non-symmetric)……..	25

Figure 4.12	Cross sectional view of the solution field at x=0 (upper view, non-symmetric)…….……..	26
Figure 4.13	Cross sectional view of the mesh in spherical polar coordinates…….	27
Figure 4.14	Cross sectional view of 3-D domain comprising the 3-D ellipsoidal body ……..	28
Figure 4.15	Cross section of MESH1 (21 x 21 x 21) ……	30
Figure 4.16	Cross section of MESH2 (21 x 21 x 21)…….	30
Figure 4.17	Cross section of MESH3 (21 x 21 x 21) ……	31
Figure 4.18	Cross section of MESH1 + MESH2 + MESH3 …….	31
Figure 4.19	Border lines of half of the multi-domain ……	32
Figure 4.20	Cross sectional view of the temperature contours obtained at the central X-plane the ellipsoid of in the multi-domain …….	33
Figure 4.21	Top view of the temperature contours of Fig.4.20 ……..	33
Figure 4.22	Chart showing the gain rate in terms of the radial mesh resolution when multi domain approach is adapted ……..…….	35
Figure 4.23	Chart showing the gain rate in terms of the overall mesh resolution when multi domain approach is adapted ……..…….	36

Figure 4.24a-b	Vector transformation from spherical coordinates (r,θ,ϕ) to Cartesian coordinates …….…….....	41
Figure 4.25	Cross sectional side view of velocity field around the 3-D ellipsoid ……..……	46
Figure 4.26a	Zoom shot of Fig. 4.25 on the leading part of the ellipsoid body ……..……..	47
Figure 4.26b	Zoom shot of Fig. 4.25 on the trailing part of the ellipsoid body ……..……..	47
Figure 4.27	Two dimensional representation of the velocity field at the centerline of the ellipsoid (z = 0) according to Viana et al. [9]…….	48
Figure 4.28	Cross sectional view of velocity field around the 3-D ellipsoid (top view) ……..…..…	49
Figure 4.29	Double cross sectional perspective view of potential field around 3-D ellipsoid ……	50
Figure 4.30a	Contours of potential function along central Z-plane …….….	51
Figure 4.30b	Contours of potential function along central Y-plane ……..….	51

LIST OF TABLES

Table 1	Comparison of single/multi domains in terms of radial resolution	34
Table 2	Comparison of single/multi domains in terms of overall resolution	35

LIST OF SYMBOLS / ABBREVIATIONS

r	Radial dimension in spherical polar coordinates
V_η	Radial velocity component in oblate sphr. coord.
V_θ	Angular velocity component in oblate sphr. coord.
V_φ	Angular velocity component in oblate sphr. coord.
V_∞	Velocity of uniform flow
ψ	Potential Function
θ	Angular dimension in spherical polar or oblate spheroidal coordinates
ϕ	Angular dimension in spherical polar coordinates
η	Radial dimension in oblate spheroidal coordinates
φ	Angular dimension in oblate spheroidal coordinates
∇^2	Laplacian Operator
ADI	Alternating Direction Implicit
ADIE	ADI coefficient at geographic east
ADIL	ADI coefficient at geographic lower position
ADIN	ADI coefficient at geographic north
ADIP	ADI coefficient at point
ADIS	ADI coefficient at geographic south
ADIU	ADI coefficient at geographic upper position
ADIW	ADI coefficient at geographic west
AE	G-S coefficient at geographic east (oblate sphere. coord.)
AL	G-S coefficient at geographic lower position (oblate sphere. coord.)
AN	G-S coefficient at geographic north (oblate sphere. coord.)
AP	G-S coefficient at point (oblate sphere. coord.)
AS	G-S coefficient at geographic south (oblate sphere. coord.)
AU	G-S coefficient at geographic upper position (oblate sphere. coord.)
AW	G-S coefficient at geographic west (oblate sphere. coord.)

grad	gradient
G-S	Gauss-Seidel
GSE	Gauss-Seidel coefficient at geographic east
GSL	Gauss-Seidel coefficient at geographic lower position
GSN	Gauss-Seidel coefficient at geographic north
GSP	Gauss-Seidel coefficient at point
GSS	Gauss-Seidel coefficient at geographic south
GSU	Gauss-Seidel coefficient at geographic upper position
GSW	Gauss-Seidel coefficient at geographic west
I.M.	Iterative Methods
NPHI	Number of nodes in ϕ direction
NR	Number of nodes in radial direction (r)
NTETA	Number of nodes in θ direction
RES	Dummy function of (η,θ,φ)

1. INTRODUCTION

An object of the present study is to numerically experiment the effects and the advantages of multi domain technique in three-dimensional spatial coordinates. It is known that this formulation produces constant-size sub-problems which may also be subject to parallel analysis. The physical structure over which air flows is a 3-D spherical and/or ellipsoidal body.

A three dimensional study in the spherical polar coordinate system and particularly, in the oblate spheroidal coordinate system was intended to simplify model problems. As all models were made 3-D, excessive computational work has to be handled in care. The governing equation becomes more complex due the 3-D nature of the problem and the coordinate system selection. A solution to the three dimensional potential flow in oblate spheroidal coordinates will be provided.

The problem of potential flow of a second-order fluid around an ellipsoid is solved in [9]. The flow fields were determined by the harmonic potential. The potential for the ellipse is a classical solution given as a complex function of a complex variable. The stress for a second-order fluid was evaluated on the irrotational flow by Viana et al. [9].

Various methods exist for the solution of Laplace Equation. Among these, there are not only numerical methods but also analytical methods that allow solution in three dimensional spaces. Burstein's [10] study confirmed that there exists the general solution of Laplace's equation in ellipsoidal coordinates which satisfies the Stäckel Theorem. His solution gives the most general form of the force function which allows the integration of equations of motion in space by separation of variables.

The concept of finite difference approximations to partial derivatives is presented at various sources e.g. in [1] or [12]. These approximations can be applied either to spatial derivatives or time derivatives. Quite general classes of meshes expressed in general curvilinear coordinates in physical space can be transformed to a uniform Cartesian mesh

with equispaced intervals in a so called computational space. The computational space is uniform. All the geometric variation is absorbed into variable coefficients of the transformed equations [12].

The basic idea of the multi grid scheme is to employ coarse grids in order to drive the solution on the finest grid faster to steady-state [7- Sec. 9.4]. Two effects are utilized for this purpose:

(*i*) Larger time steps can be employed on the coarser grids in conjunction with a reduced numerical effort. Since the work for determining a new solution is distributed mainly over the coarser grids, a more rapid convergence and a reduction of the computing time results.

(*ii*) The majority of the explicit and implicit time-stepping and iterative schemes reduce efficiently mainly the high-frequency components of the solution error. The low-frequency components are usually only hardly damped. This result in a slow convergence to the steady state, after the initial phase (where the largest errors are eliminated) is over. The multi grid scheme helps at this point -the low-frequency components of the finest grid becomes high-frequency components on the coarser grids and are successively damped. As a result, the entire error is very quickly reduced, and the convergence is significantly accelerated [7].

The numerical simulation of external flows past airfoils, wings, cars and other configurations has to be conducted within a bounded domain. For this reason, artificial far field boundary conditions become necessary. The numerical implementation of the far field boundary conditions has to fulfill two basic requirements. First, the truncation of the domain should have no notable effects on the flow solution as compared to the infinite domain. Second, any outgoing disturbances must not be reflected back into the flow field [9]. Due to their elliptic nature, sub- and transonic flow problems are particularly sensitive to the far field boundary conditions. An inadequate implementation can lead to a significant slow down of convergence to the steady state. Furthermore, the accuracy of the solution is likely to be negatively influenced [7- Sec. 8.3].

In most three dimensional cases, the problem involves boundary cuts. The coordinate cut represents an artificial, not a physical, boundary. It is a line (plane in 3D) composed of grid points with different computational coordinate(s) but the same physical location. This means that the grid is folded such that it touches itself. The coordinate cut appears for the so-called C- or 0-grid topology. The flow variables and their gradients have to stay continuous across the cut [7- Sec. 8.6].

The idea of systematically using sets of coarser grids to accelerate the convergence of iterative schemes that arise from the numerical solution to partial differential equations was used long ago. However, one should also know that there are many variations of the process and many viewpoints of the underlying theory.

Many iterative methods reduce error components corresponding to eigenvalues of large amplitude more effectively than those corresponding to eigenvalues of small amplitude. This is to be expected of an iterative method which is time accurate. It is also true for example of the Gauss-Seidel method and by design of the Richardson method. The classical point Jacobi method does not share this property [12].

Yaldizli [6] studied multiple-domain analysis of unsteady combustion with detailed chemistry for a spherical fuel source. He derived a numerical solution to the governing equations for incompressible and laminar flow in two-dimensional spherical polar coordinates, adopting the two dimensional stream function vorticity formulation. He also incorporated multiple-domain analysis (domain decomposition) into his study.

The following chapters outline the study made as part of the Graduate Program and does not include the source codes written for the solution of 3-D potential function.

2. MATHEMATICAL MODELING IN SPHERICAL POLAR COORDINATE SYSTEM

Potential flow is governed by a second order partial differential equation of elliptic type, namely the well known Laplace equation;

$$\nabla^2\psi = 0 \tag{2.1}$$

where

$$\psi = \psi(r,\theta,\phi) \tag{2.2}$$

denotes the potential function in three spatial dimensions in which

$$0 \le r \le \infty$$
$$0 \le \theta \le \pi$$
$$0 \le \phi \le 2\pi$$

Attention shall be paid to the fact that ϕ spans from 0 to 2π radians while θ spans from 0 to π radians only. Conversion from spherical polar coordinates to the Cartesian coordinates can be made using the following equations [8];

$$x = rSin(\theta)Cos(\phi) \tag{2.3}$$
$$y = rSin(\theta)Sin(\phi) \tag{2.4}$$
$$z = rCos(\theta) \tag{2.5}$$

The Laplace equation of Eqn. (2.1) expressed in the spherical polar coordinates takes the form [5] ;

$$\frac{\partial^2\psi}{\partial r^2} + \frac{2}{r}\frac{\partial\psi}{\partial r} + \frac{1}{r^2}\frac{\partial^2\psi}{\partial\theta^2} + \frac{Cot(\theta)}{r^2}\frac{\partial\psi}{\partial\theta} + \frac{1}{r^2Sin^2(\theta)}\frac{\partial^2\psi}{\partial\phi^2} = 0 \tag{2.6}$$

Trigonometric terms in the denominators of Eqn.(4) poses a major problem in the numerical calculations and hence shall be removed from the equation as these will lead to

singularities at e.g. θ = 0 in the discretized form of Eqn.(4). Multiplying both sides of Eqn. (4) by $r^2 \sin^2(\theta)$ leads to;

$$r^2 Sin^2(\theta)\frac{\partial^2\psi}{\partial r^2} + 2rSin^2(\theta)\frac{\partial\psi}{\partial r} + Sin^2(\theta)\frac{\partial^2\psi}{\partial\theta^2} + Sin(\theta)Cos(\theta)\frac{\partial\psi}{\partial\theta} + \frac{\partial^2\psi}{\partial\phi^2} = 0 \qquad (2.7)$$

Eqn. (2.7) is now ready for a finite difference discretization. Using a first order central difference approximation;

$$\begin{aligned} r_{i,j,k}^2 Sin^2(\theta_{i,j,k})\frac{\psi_{i+1,j,k} - 2\psi_{i,j,k} + \psi_{i-1,j,k}}{\Delta r_{i,j,k}^2} + 2r_{i,j,k}Sin^2(\theta_{i,j,k})\left(\frac{\psi_{i+1,j,k} - \psi_{i-1,j,k}}{2\Delta r_{i,j,k}}\right) \\ + Sin^2(\theta_{i,j,k})\frac{\psi_{i,j+1,k} - 2\psi_{i,j,k} + \psi_{i,j-1,k}}{\Delta\theta_{i,j,k}^2} + Sin(\theta_{i,j,k})Cos(\theta_{i,j,k})\frac{\psi_{i,j+1,k} - \psi_{i,j-1,k}}{2\Delta\theta_{i,j,k}} \\ + \frac{\psi_{i,j,k+1} - 2\psi_{i,j,k} + \psi_{i,j,k-1}}{\Delta\phi^2} = 0 \end{aligned} \qquad (2.8)$$

The solution to Eqn. (2.8) can be obtained by adopting one of a number of iteration methods including Jacobi I.M., The Gauss Seidel I.M. (G-S), Successive Over Relaxation I.M., (PSOR, LSOR) or and Alternating Direction Implicit I.M. (ADI) [1].

2.1 The Alternating Direction Implicit (ADI) Method

In order to establish simplicity in designating terms, Eqn. (2.8) will be divided into parts abbreviated with [ADI] coefficients and suffixed with the first letter [e.g. N(orth) or W(est)] of the geographic location of the concerned coefficient.

$$\psi_{i,j,k} \rightarrow \frac{-2r^2Sin^2(\theta)}{\Delta r^2} + \frac{-2Sin^2(\theta)}{\Delta\theta^2} + \frac{-2}{\Delta\phi^2} \rightarrow ADIP(coeff.at\ Po\text{int})$$

$$\psi_{i+1,j,k} \rightarrow \frac{rSin^2(\theta)}{\Delta r} + \frac{r^2Sin^2(\theta)}{\Delta r^2} \rightarrow ADIE(coeff.at\ East)$$

$$\psi_{i-1,j,k} \rightarrow \frac{-rSin^2(\theta)}{\Delta r} + \frac{r^2 Sin^2(\theta)}{\Delta r^2} \rightarrow ADIW\,(coeff.at\,West)$$

$$\psi_{i,j+1,k} \rightarrow \frac{Cos(\theta)Sin(\theta)}{2\Delta\theta} + \frac{Sin^2(\theta)}{\Delta\theta^2} \rightarrow ADIN\,(coeff.at\,North)$$

$$\psi_{i,j-1,k} \rightarrow \frac{-Cos(\theta)Sin(\theta)}{2\Delta\theta} + \frac{Sin^2(\theta)}{\Delta\theta^2} \rightarrow ADIS\,(coeff.at\ South)$$

$$\psi_{i,j,k+1} \rightarrow \frac{1}{\Delta\phi^2} \rightarrow ADIU\,(coeff.at\,Upper\,location)$$

$$\psi_{i,j,k-1} \rightarrow \frac{1}{\Delta\phi^2} \rightarrow ADIL\,(coeff.at\,Lower\,location)$$

Equation (2.8), the well known Laplace Equation, can now be expressed in discrete form;

$$ADIP \bullet \psi_{i,j,k} + ADIW \bullet \psi_{i-1,j,k} + ADIE \bullet \psi_{i+1,j,k} + ADIN \bullet \psi_{i,j+1,k}$$

$$+ ADIS \bullet \psi_{i,j-1,k} + ADIU \bullet \psi_{i,j,k+1} + ADIL \bullet \psi_{i,j,k} = 0 \qquad (2.9)$$

Unlike many iteration schemes, a single cycle in the Alternating Direction Implicit (ADI) Method can be completed in three distinct sweeps in the three ordinates (r, θ, ϕ) of the coordinate system [1]. Each time a sweep is arranged, all points that are not located in the direction of the sweep are assumed to be known values from the previous iteration cycle. These values are hence placed on the right side of the equation (2.9) at each cycle. Apparently, these sweeps have to be handled separately. An iteration cycle is considered complete once the resulting tridiagonal system is solved for all the rows and then followed by columns, or vice versa [Ref. 1 section 5.3.6.]. We will now explore ADI Sweeps (r,θ,φ);

(i) Sweep-r

$$ADIW \bullet \psi_{i-1,j,k}^{n+1/3} + ADIP \bullet \psi_{i,j,k}^{n+1/3} + ADIE \bullet \psi_{i+1,j,k}^{n+1/3} =$$
$$-\left(ADIN \bullet \psi_{i,j+1,k} + ADIS \bullet \psi_{i,j-1,k}^{n+1/3} + ADIU \bullet \psi_{i,j,k+1}^{n+1/3} + ADIL \bullet \psi_{i,j,k-1}^{n+1/3} \right) \quad (2.10)$$

The superscript n+1/3 indicates the first of the three sweeps.

(ii) Sweep- θ

$$ADIS \bullet \psi_{i,j-1,k}^{n+2/3} + ADIP \bullet \psi_{i,j,k}^{n+2/3} + ADIN \bullet \psi_{i,j+1,k}^{n+2/3} =$$
$$-\left(ADIW \bullet \psi_{i-1,j,k}^{n+2/3} + ADIE \bullet \psi_{i+1,j,k}^{n+2/3} + ADIU \bullet \psi_{i,j,k+1}^{n+2/3} + ADIL \bullet \psi_{i,j,k-1}^{n+2/3} \right) \quad (2.11)$$

The superscript n+2/3 indicates the second of the three sweeps.

(iii) Sweep - ϕ

$$ADIL \bullet \psi_{i,j,k-1}^{n+1} + ADIP \bullet \psi_{i,j,k}^{n+1} + ADIU \bullet \psi_{i,j,k+1}^{n+1} =$$
$$-\left(ADIW \bullet \psi_{i-1,j,k}^{n+1} + ADIE \bullet \psi_{i+1,j,k}^{n+1} + ADIN \bullet \psi_{i,j+1,k}^{n+1} + ADIS \bullet \psi_{i,j-1,k}^{n+1} \right) \quad (2.12)$$

The superscript n+1 indicates the third of the three sweeps.

In these equations, Eqn. (2.10) is solved implicitly for the unknown in the **r** direction, Eqn. (2.11) is solved implicitly for the unknown in the **θ** direction and Eqn.(2.12) is solved implicitly for the unknown in the **ϕ** direction.

It is apparent that the resulting system will form a tridiagonal system whose first element on the first row and the last element in the last row are known values from the boundary conditions. These known values are to be carried to the right side vector of known values and subtracted from the corresponding elements of the vector [D]. The vector formed by the main diagonal of the coefficients matrix is designated as vector [B],

while the other two diagonals found on the lower and upper parts of the main diagonal are designated as vectors [A] and [C] respectively. The resulting system can be illustrated in the following way;

$$\begin{bmatrix} A_1 & \begin{bmatrix} B_1 & C_1 & & & & & & & \\ A_2 & B_2 & C_2 & & & & & & \\ & A_3 & B_3 & C_3 & & & & & \\ & & \ddots & \ddots & \ddots & & & & \\ & & & & & \ddots & \ddots & & \\ & & & & & \ddots & B_{NR-2} & C_{NR-2} & \\ & & & & & & A_{NR-1} & B_{NR-1} & C_{NR-1} \\ & & & & & & & A_{NR} & B_{NR} \end{bmatrix} & C_{NR} \end{bmatrix} \begin{bmatrix} \psi_1 \\ \psi_2 \\ \psi_3 \\ \vdots \\ \\ \\ \vdots \\ \psi_{NR-2} \\ \psi_{NR-1} \\ \psi_{NR} \end{bmatrix} = \begin{bmatrix} D_1 \\ D_2 \\ D_3 \\ \\ \\ \\ \\ D_{NR-2} \\ D_{NR-1} \\ D_{NR} \end{bmatrix}$$

in which dimensions of the coefficients matrix is (NR-2) x (NR) in its original form. Once the known boundary values A_1 and C_{NR} are carried to the right hand side vector [D], the resulting tridiagonal matrix becomes an (NR-2) x (NR-2) in dimension. NR is the number of nodes in the r-direction. This will be replaced by NTETA and NPHI in the subsequent θ and ϕ sweeps. If we read the rows of the coefficients matrix, we find that ;

$$\begin{aligned} i = 2 \quad &\rightarrow \quad ADIW\psi_1 + ADIP\psi_2 + ADIE\psi_3 = -(ADIN\psi_2 \cdots\cdots) \\ i = 3 \quad &\rightarrow \quad ADIW\psi_2 + ADIP\psi_3 + ADIE\psi_4 = -(ADIN\psi_3 \cdots\cdots) \\ &\vdots \qquad\qquad\qquad\qquad \vdots \\ &\vdots \qquad\qquad\qquad\qquad \vdots \\ i = NR-1 \quad &\rightarrow \quad ADIW\psi_{NR-2} + ADIP\psi_{NR-1} + ADIE\psi_{NR} = -(ADIN\psi_{NR-2} \cdots\cdots) \end{aligned}$$

Re-arranging terms of the coefficients matrix, we obtain the following system of equations;

$$\begin{bmatrix} B_1 & C_1 & & & & & & & \\ A_2 & B_2 & C_2 & & & & & & \\ & A_3 & B_3 & C_3 & & & & & \\ & & \ddots & \ddots & \ddots & & & & \\ & & & & & \ddots & \ddots & \ddots & \\ & & & & & & A_{NR-1} & B_{NR-1} & C_{NR-1} \\ & & & & & & & A_{NR} & B_{NR} \end{bmatrix} \begin{bmatrix} \psi_2 \\ \psi_3 \\ \psi_4 \\ \vdots \\ \\ \\ \\ \vdots \\ \psi_{NR-2} \\ \psi_{NR-1} \end{bmatrix} = \begin{bmatrix} d_1 - A_1\psi_1 \\ d_2 \\ d_3 \\ \\ \\ \\ \\ \\ d_{NR-1} \\ d_{NR-2} - C_{NR-2}\psi_{NR} \end{bmatrix} \quad (2.13)$$

Having applied the boundary conditions, the system of equations can now be expressed as

$$[A]_{(NR-2)(NR-2)} \times [\psi]_{(NR-2)} = [d]_{(NR-2)} \quad (2.14)$$

The same procedure shall be applied for the θ and the ϕ sweeps. It should be noted that the resulting tridiagonal system shall be solved by a tridiagonal matrix solver each time a sweep is completed. As these steps are apparent from the previously followed steps outlined above, no more description will be brought with regards to the implementation of the θ and the ϕ sweeps.

2.2 Gauss Seidel Iteration Scheme

We will revert to Eqn. (2.9) for illustrating the Gauss-Seidel (G-S) iteration scheme and rewrite the same using a slightly different notation for the coefficients. These will be as follows:

$$\psi_{i,j,k} \rightarrow \frac{-2r^2 Sin^2(\theta)}{\Delta r^2} + \frac{-2Sin^2(\theta)}{\Delta\theta^2} + \frac{-2}{\Delta\phi^2} \rightarrow GSP(coeff.at\ Po\text{int})$$

$$\psi_{i+1,j,k} \rightarrow \frac{rSin^2(\theta)}{\Delta r} + \frac{r^2 Sin^2(\theta)}{\Delta r^2} \rightarrow GSE(coeff.at\ East)$$

$$\psi_{i-1,j,k} \rightarrow \frac{-rSin^2(\theta)}{\Delta r} + \frac{r^2 Sin^2(\theta)}{\Delta r^2} \rightarrow GSW\,(coeff.at\,West)$$

$$\psi_{i,j+1,k} \rightarrow \frac{Cos(\theta)Sin(\theta)}{2\Delta\theta} + \frac{Sin^2(\theta)}{\Delta\theta^2} \rightarrow GSN\,(coeff.at\,North)$$

$$\psi_{i,j-1,k} \rightarrow \frac{-Cos(\theta)Sin(\theta)}{2\Delta\theta} + \frac{Sin^2(\theta)}{\Delta\theta^2} \rightarrow GSS\,(coeff.at\ South)$$

$$\psi_{i,j,k+1} \rightarrow \frac{1}{\Delta\phi^2} \rightarrow GSU\,(coeff.at\,Upper\,location)$$

$$\psi_{i,j,k-1} \rightarrow \frac{1}{\Delta\phi^2} \rightarrow GSL\,(coeff.at\,Lower\,location)$$

Rewriting the governing Laplace equation in discrete form with these coefficients, Eqn (2.9) takes the form;

$$GSP \bullet \psi_{i,j,k} + GSW \bullet \psi_{i-1,j,k} + GSE \bullet \psi_{i+1,j,k} + GSN \bullet \psi_{i,j+1,k} + GSS \bullet \psi_{i,j-1,k} + GSU \bullet \psi_{i,j,k+1} + GSL \bullet \psi_{i,j,k} = 0 \qquad (2.15)$$

and rearranging terms, we obtain the expression for the potential function ψ,

$$\psi_{i,j,k}^{m+1} = \frac{-1}{GSP}[GSW \bullet \psi_{i-1,j,k} + GSE \bullet \psi_{i+1,j,k} + GSN \bullet \psi_{i,j+1,k} + GSS \bullet \psi_{i,j-1,k} + GSU \bullet \psi_{i,j,k+1} + GSL \bullet \psi_{i,j,k}]^m \qquad (2.16)$$

According to Eqn. (2.16), the potential function $\psi_{i,j,k}$ will be updated at every iteration cycle m. A relaxation parameter can be introduced into (2.16) in order to accelerate the solution and provide faster convergence. As the Gauss-Seidel iteration is scheme is a well-known numerical technique and can be found in various sources in

varying complexity e.g. in [1] or more particularly, incorporated with extensive multi-grid methods in [2], no longer description of will be given here.

3. MATHEMATICAL MODELING IN OBLATE SPHEROIDAL COORDINATE SYSTEM

As was mentioned in Chapter 2 above, potential flow is governed by the elliptic second order partial differential equation, the Laplace equation;

$$\nabla^2\psi = 0 \tag{3.1}$$

where

$$\psi = \psi(\eta, \theta, \varphi) \tag{3.2}$$

denotes the potential function in three spatial dimensions in which

$$0 \le \eta \le \infty$$
$$0 \le \theta \le \pi$$
$$0 \le \varphi \le 2\pi$$

Attention shall be paid to the fact that φ spans from 0 to 2π radians while θ spans from 0 to π radians only. Conversion from oblate spheroidal coordinates to the Cartesian coordinates can be made using the following equations;

$$x = aCosh(\eta)Sin(\theta)Cos(\varphi) \tag{3.3}$$
$$y = aCosh(\eta)Sin(\theta)Sin(\varphi) \tag{3.4}$$
$$z = aSinh(\eta)Cos(\theta) \tag{3.5}$$

where a is the focus on the primary axis. The Laplace equation of Eqn. (3.1) expressed in the spherical polar coordinates takes the form [5-pp.32] ;

$$\nabla^2\psi = \frac{1}{a^2\left(Cosh^2(\eta) - Sin^2(\theta)\right)}\left[\frac{\partial^2\psi}{\partial\eta^2} + Tanh(\eta)\frac{\partial\psi}{\partial\eta} + \frac{\partial^2\psi}{\partial\theta^2} + Cot(\theta)\frac{\partial\psi}{\partial\theta}\right]$$

$$+\frac{1}{a^2 Cosh^2(\eta)Sin^2(\theta)}\frac{\partial^2\psi}{\partial\varphi^2} \qquad (3.6)$$

As in the case of spherical polar coordinates, the solution to the governing equation (3.6) can be obtained by adopting one of a number of iteration methods including Jacobi I.M., The Gauss Seidel I.M. (G-S), Successive Over Relaxation I.M. (PSOR, LSOR) or and Alternating Direction Implicit I.M. (ADI).

Before starting discretization of Eqn. (3.6), let us first simplify the equation by multiplying both sides by

$$a^2 Cosh^2(\eta)Sin^2(\theta)$$

after which we obtain ;

$$\frac{Cosh^2(\eta)Sin^2(\theta)}{Cosh^2(\eta) - Sin^2(\theta)}\left[\frac{\partial^2\psi}{\partial\eta^2} + Tanh(\eta)\frac{\partial\psi}{\partial\eta} + \frac{\partial^2\psi}{\partial\theta^2} + Cot(\theta)\frac{\partial\psi}{\partial\theta}\right] + \frac{\partial^2\psi}{\partial\varphi^2} = 0 \qquad (3.7)$$

In order to further simplify the discretization, let us assign a dummy function $Q(\eta,\theta)$

$$Q(\eta,\theta) = \frac{Cosh^2(\eta)Sin^2(\theta)}{Cosh^2(\eta) - Sin^2(\theta)} \qquad (3.8)$$

Once we insert the dummy function of (3.8) in Eqn. (3.7) and discretize the same, we obtain;

$$Q(\eta,\theta)\left[\frac{\psi_{i-1,j,k} - 2\psi_{i,j,k} + \psi_{i+1,j,k}}{(\Delta\eta)^2} + Tanh(\eta)\left(\frac{\psi_{i-1,j,k} - \psi_{i+1,j,k}}{2\Delta\eta}\right)\right.$$

$$\left. + \frac{\psi_{i,j-1,k} - 2\psi_{i,j,k} + \psi_{i,j+1,k}}{(\Delta\theta)^2} + Cot(\theta)\frac{\psi_{i,j-1,k} - \psi_{i,j+1,k}}{2\Delta\theta}\right]$$

$$+\frac{\psi_{i,j,k-1} - 2\psi_{i,j,k} + \psi_{i,j,k+1}}{(\Delta\varphi)^2} = 0 \qquad (3.9)$$

We will first multiply each sides of Eqn. (3.9) by Sin(θ) and sort all potential function terms according to their geographic locations in the computational space. Rewriting equation (21) yields;

$$\begin{aligned}
&\left[\frac{Q(\eta,\theta)Sin(\theta)}{(\Delta\eta)^2}+\frac{Q(\eta,\theta)Tanh(\eta)Sin(\theta)}{2\Delta\eta}\right]\psi_{i-1,j,k}\\
&+\left[\frac{Q(\eta,\theta)Sin(\theta)}{(\Delta\eta)^2}+\frac{Q(\eta,\theta)Tanh(\eta)Sin(\theta)}{2\Delta\eta}\right]\psi_{i+1,j,k}\\
&+\left[\frac{Q(\eta,\theta)Sin(\theta)}{(\Delta\theta)^2}+\frac{Q(\eta,\theta)Cos(\theta)}{2\Delta\theta}\right]\psi_{i,j-1,k}\\
&+\left[\frac{Q(\eta,\theta)Sin(\theta)}{(\Delta\theta)^2}+\frac{Q(\eta,\theta)Cos(\theta)}{2\Delta\theta}\right]\psi_{i,j+1,k}\\
&+\left[\frac{Sin(\theta)}{(\Delta\varphi)^2}\right]\psi_{i,j,k-1}+\left[\frac{Sin(\theta)}{(\Delta\varphi)^2}\right]\psi_{i,j,k+1}\\
&+\left[\frac{-2Q(\eta,\theta)Sin(\theta)}{(\Delta\eta)^2}+\frac{-2Q(\eta,\theta)Sin(\theta)}{(\Delta\theta)^2}+\frac{-2Sin(\theta)}{(\Delta\varphi)^2}\right]\psi_{i,j,k}=0
\end{aligned}\qquad(3.10)$$

For simplicity, the coefficients to each potential function term ψ will be designated as follows ;

$$AP=\left[\frac{-2Q(\eta,\theta)Sin(\theta)}{(\Delta\eta)^2}+\frac{-2Q(\eta,\theta)Sin(\theta)}{(\Delta\theta)^2}+\frac{-2Sin(\theta)}{(\Delta\varphi)^2}\right]$$

$$AW=\left[\frac{Q(\eta,\theta)Sin(\theta)}{(\Delta\eta)^2}+\frac{Q(\eta,\theta)Tanh(\eta)Sin(\theta)}{2\Delta\eta}\right]$$

$$AE=\left[\frac{Q(\eta,\theta)Sin(\theta)}{(\Delta\eta)^2}+\frac{Q(\eta,\theta)Tanh(\eta)Sin(\theta)}{2\Delta\eta}\right]$$

$$AS=\left[\frac{Q(\eta,\theta)Sin(\theta)}{(\Delta\theta)^2}+\frac{Q(\eta,\theta)Cos(\theta)}{2\Delta\theta}\right]$$

$$AN = \left[\frac{Q(\eta,\theta)Sin(\theta)}{(\Delta\theta)^2} + \frac{Q(\eta,\theta)Cos(\theta)}{2\Delta\theta} \right]$$

$$AU = \left[\frac{Sin(\theta)}{(\Delta\varphi)^2} \right] \qquad \text{and} \qquad AL = \left[\frac{Sin(\theta)}{(\Delta\varphi)^2} \right]$$

Applying the Gauss-Seidel Iteration Scheme to Eqn. (3.10), we obtain the discrete form of the governing equation which can now be easily implemented iteratively in a code.

$$\psi_{i,j,k} = \frac{-1}{AP}\left[(AW)\psi_{i-1,j,k} + (AE)\psi_{i+1,j,k} + (AS)\psi_{i,j-1,k} + (AN)\psi_{i,j+1,k} + (AL)\psi_{i,j,k-1} + (AU)\psi_{i,j,k+1} \right] \tag{3.11}$$

4. COMPUTATIONAL RESULTS

A FORTRAN code was written to solve a number of 3-D problems. The code has various modules to produce meshes in spherical polar coordinates or oblate spheroidal coordinates and obtain solution of the potential function using the mathematical modeling obtained in previous sections. Starting from a relatively simple case, the solution will proceed towards a three dimensional potential flow over an ellipsoidal body.

4.1 Solution of the Potential Function in 3-D Spherical Polar Coordinates

We will now revert back to Eqn. (2.16) and rewrite the same for solution of the three dimensional potential function ψ.

$$\psi_{i,j,k}^{m+1} = \frac{-1}{GSP}[\,GSW \bullet \psi_{i-1,j,k} + GSE \bullet \psi_{i+1,j,k} + GSN \bullet \psi_{i,j+1,k} + GSS \bullet \psi_{i,j-1,k} + GSU \bullet \psi_{i,j,k+1} + GSL \bullet \psi_{i,j,k}\,]^{m} \qquad (4.1)$$

Open forms of the coefficients GSW, GSE, GSN, GSS, GSU, GSL and GSP are already given in Chapter 2.2. We will now assume a domain in between the two 3-D shells. The smaller sphere located inside the larger sphere is assumed to be a solid body. The elliptic PDE will be solved on the volume in between the two spheres.

Fig. 4.1 shows a sample domain having, for simplicity, 21 x 21 x 21 nodes;

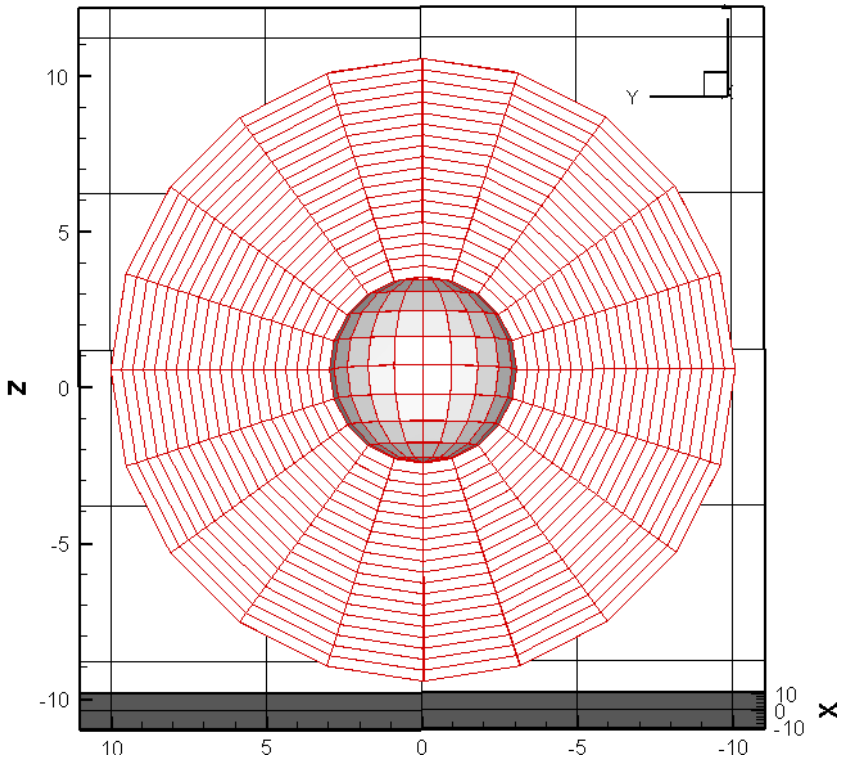


Fig. 4.1 Cross sectional view of the spherical domain

To better illustrate the domain, we will provide a perspective view of the cross section of the mesh of Fig. 4.1 in Fig. 4.2.

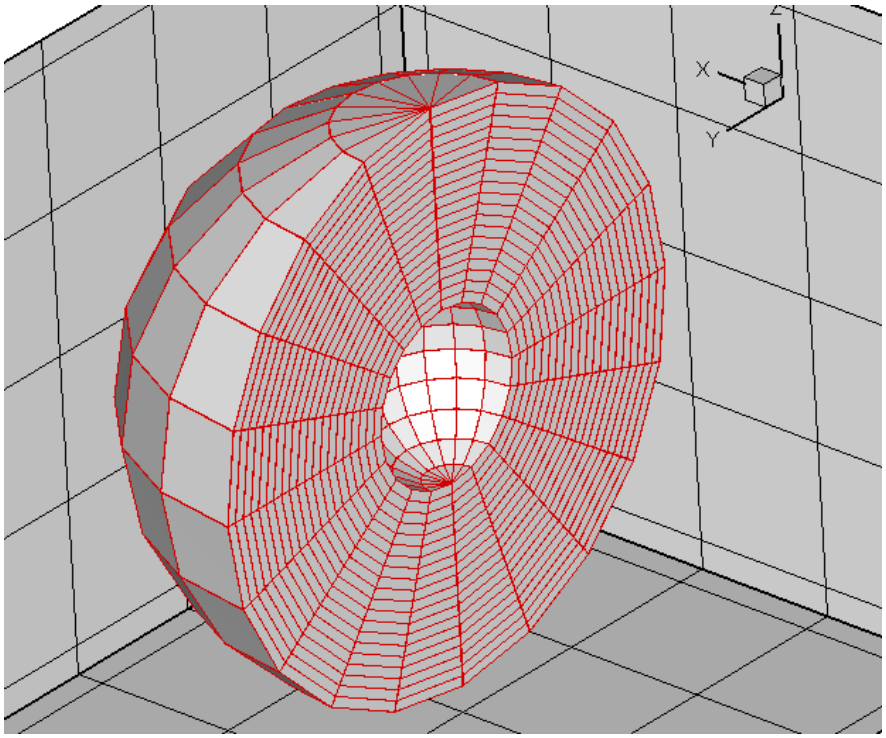


Fig.4. 2 Perspective view of the cross sectional mesh of Fig. 4.1

As smaller sphere is assumed to be a solid body, the inner volume of the smaller sphere is out of interest in the present case. The reader shall note that the inner sphere appears to be hollow hemisphere on the perspective view of Fig. 4.2.

This test case can be assumed to be heat-conduction problem within the volume in between the two shells. A FORTRAN code has been developed to implement the iterative cycle of Eqn. (4.1). The code generates the 3-D mesh in desired resolution and implements the routine to obtain the solution of the potential function. The following boundary conditions were used;

Temperature on the surface of the inner sphere: 30°C

Temperature on the surface of the outer sphere: 100°C

The inner sphere has a radius of 3 cm whereas the outer sphere has a radius of 8 cm. An initial guess of 40°C was assumed at all nodes except the inner surface of the larger sphere and the outer surface of the smaller sphere. A 2-D representation of the cross sectional view of the solution is graphically shown in Fig. 4.3;

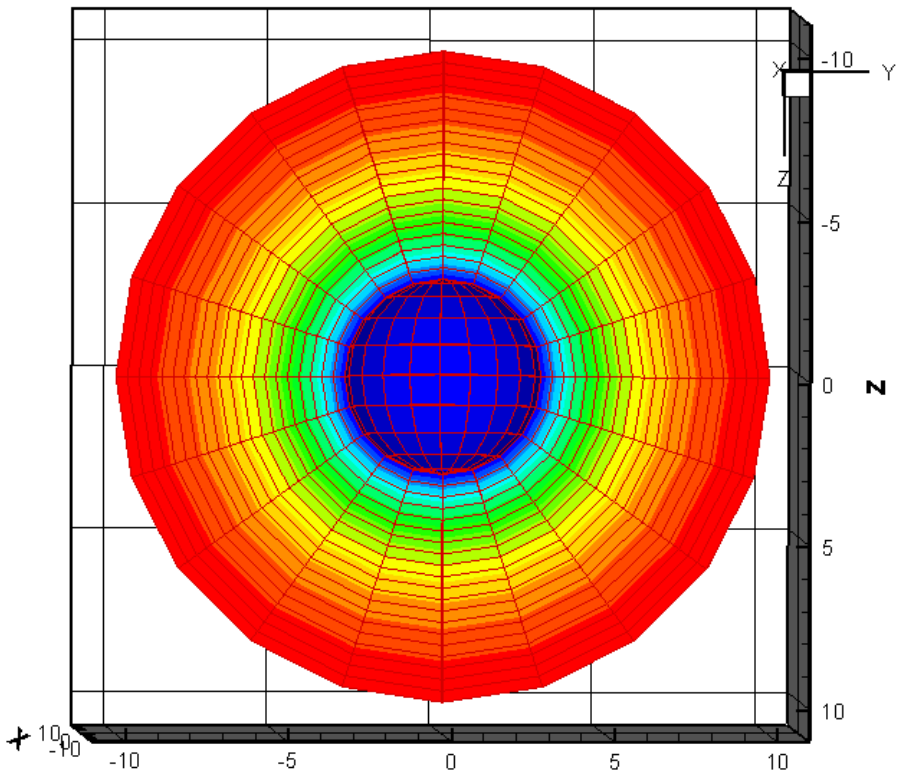


Fig. 4.3 Graphical representation of the solution for 3-D temperature field

The perspective view of the graphical representation of Fig. 4.3 is given in Fig. 4.4 :

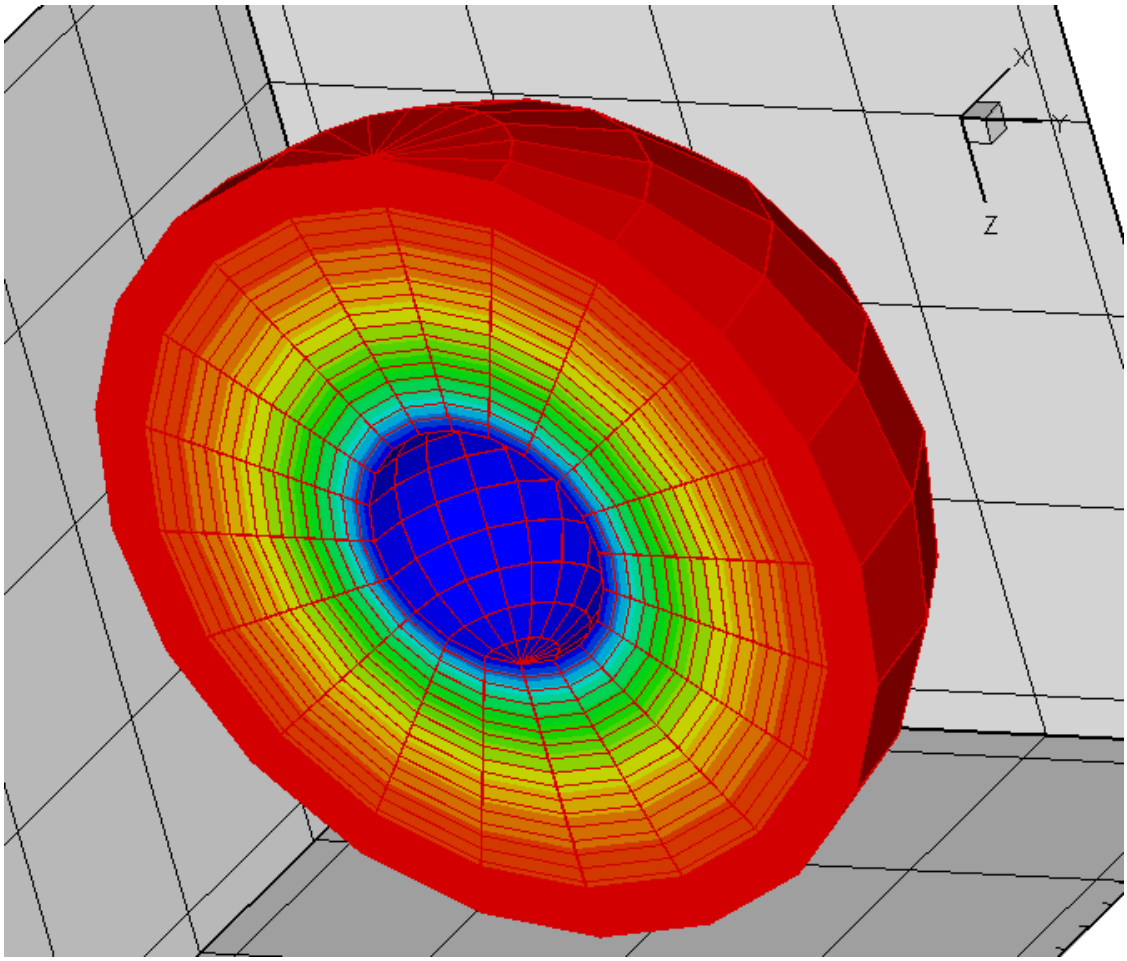


Fig. 4.4 Perspective view of the graphical representation of Fig. 4.3

The surface of the outer sphere, which is assumed to be constant at T=100°C is represented with the red color. The surface of the inner sphere, which is assumed to be constant at T=30°C is represented with the blue color. The uniform and symmetric distribution of the colors of Fig. 4.3 was the expected outcome of the code. The hollow cavity in the center of the graphical representation of Fig. 4.4 represents the cold surface of the solid body in the center of the domain.

In order to show that temperature field is distributed homogenously at any other cross section of the 3-D space, the solution field is cut around three axis at varying locations and angles to provide an arbitrary cross volume. A graphical representation of this cross volume is shown in Fig. 4.5.

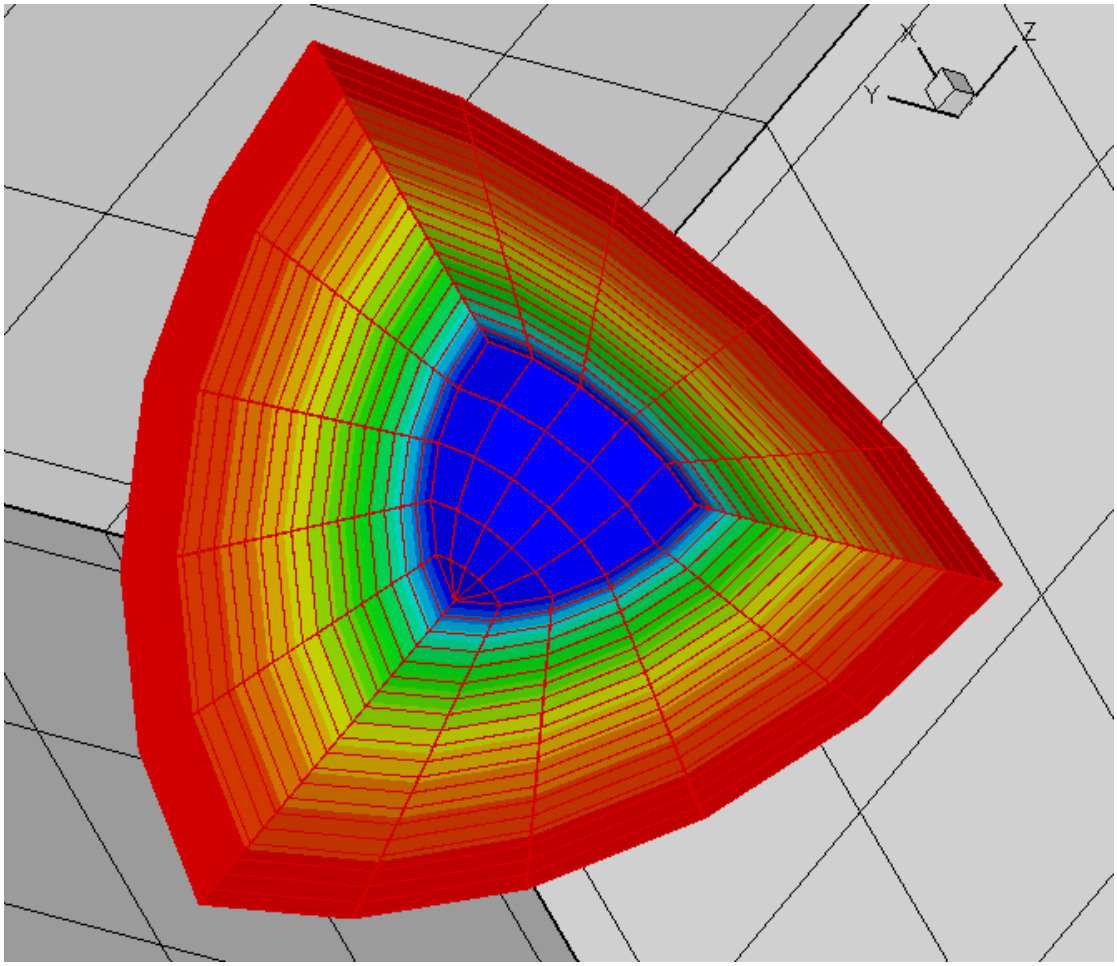


Fig. 4.5 A graphical representation of a cross volume

The uniform distribution of temperature contours of Fig. 4.5 was an expected result.

4.2 Solution of the Potential Function in 3-D Oblate Spheroidal Coordinates

We will now revert back to Eqn. (3.11) and rewrite the same for solution of the three dimensional potential function ψ in the oblate spheroidal coordinates.

$$\psi_{i,j,k} = \frac{-1}{AP}\left[(AW)\psi_{i-1,j,k} + (AE)\psi_{i+1,j,k} + (AS)\psi_{i,j-1,k} + (AN)\psi_{i,j+1,k} + (AL)\psi_{i,j,k-1} + (AU)\psi_{i,j,k+1}\right] \quad (4.2)$$

Open forms of the coefficients AW, AE, AN, AS, AU, AL and AP are already given in Chapter 3. We will now assume a domain whose outer borders are defined by a sphere and inner borders are defined by an ellipsoid located in the center of the outer sphere. The elliptic PDE will be solved on the volume in between the 3-D ellipsoid and the outer sphere.

Fig. 4.6 shows a sample domain having 21 x 21 x 21 nodes

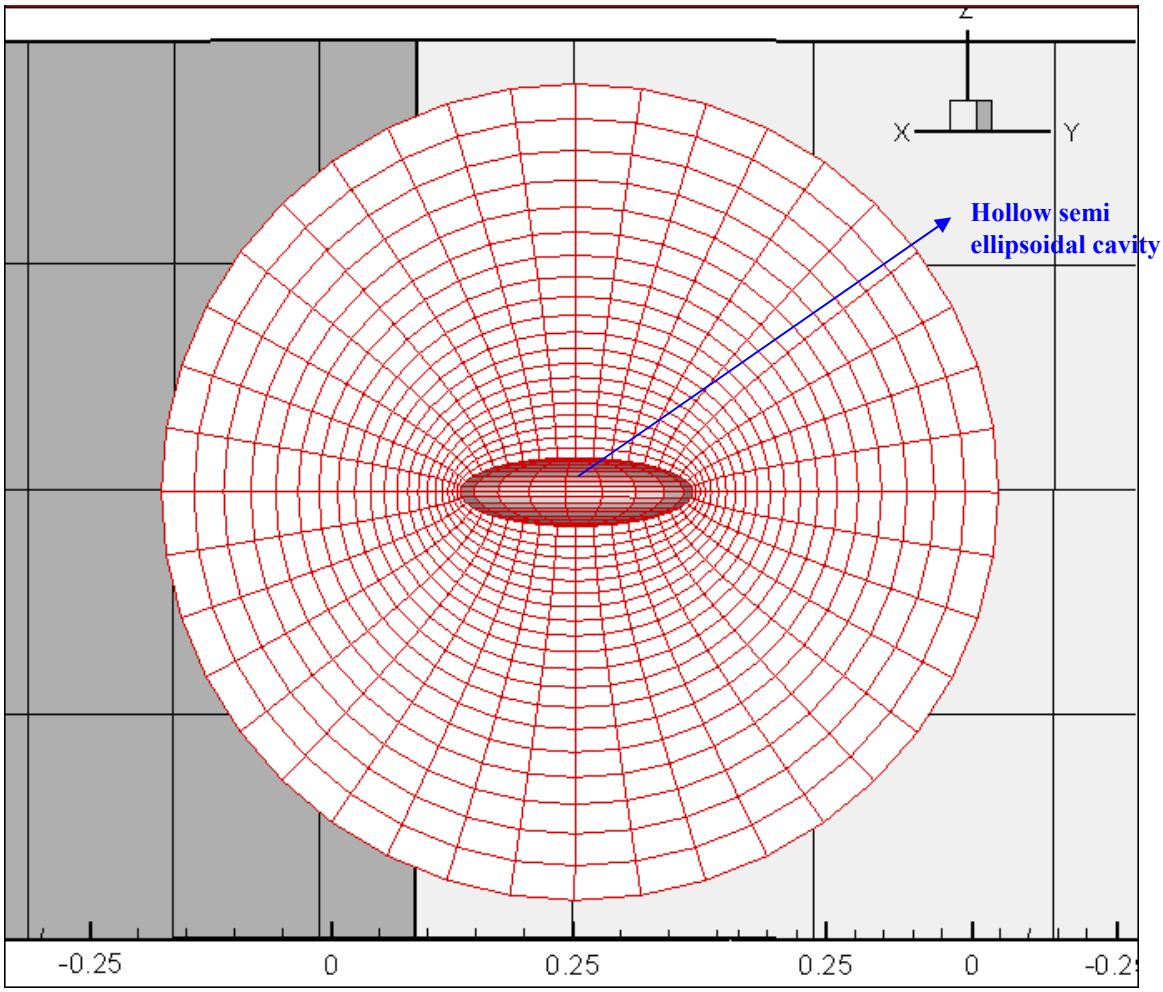


Fig. 4.6 Cross sectional view of 3-D domain comprising the 3-D ellipsoidal body

To better illustrate the domain, we will provide a perspective view of the cross section of the mesh of Fig. 4.6 in Fig. 4.7.

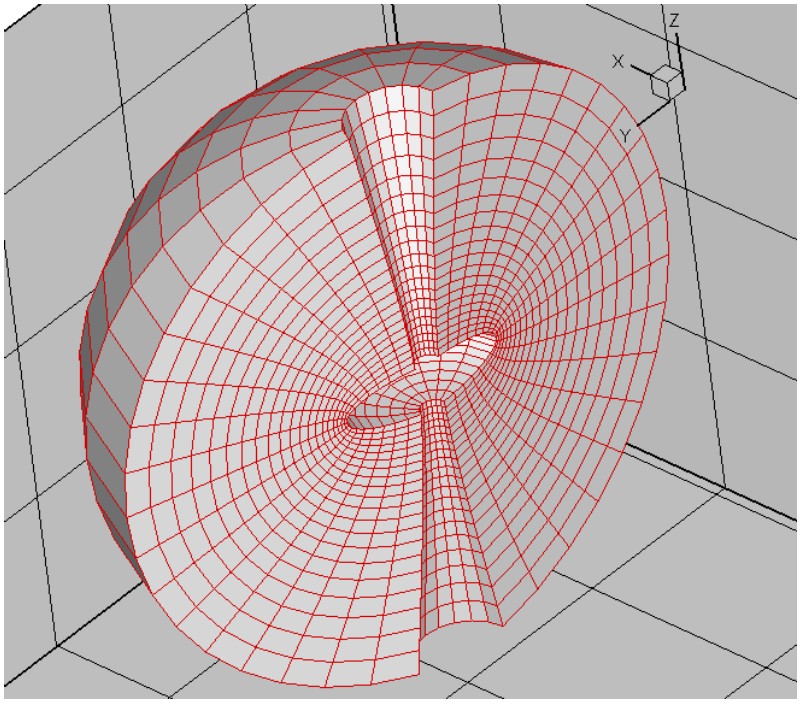


Fig. 4.7 Perspective view of the cross sectional mesh of Fig. 4.6

The ellipsoid is assumed to be solid object and hence the inside of it is not a part of the domain. The ellipsoid is therefore shown as a half cavity which extends depth-wise towards the sheet.

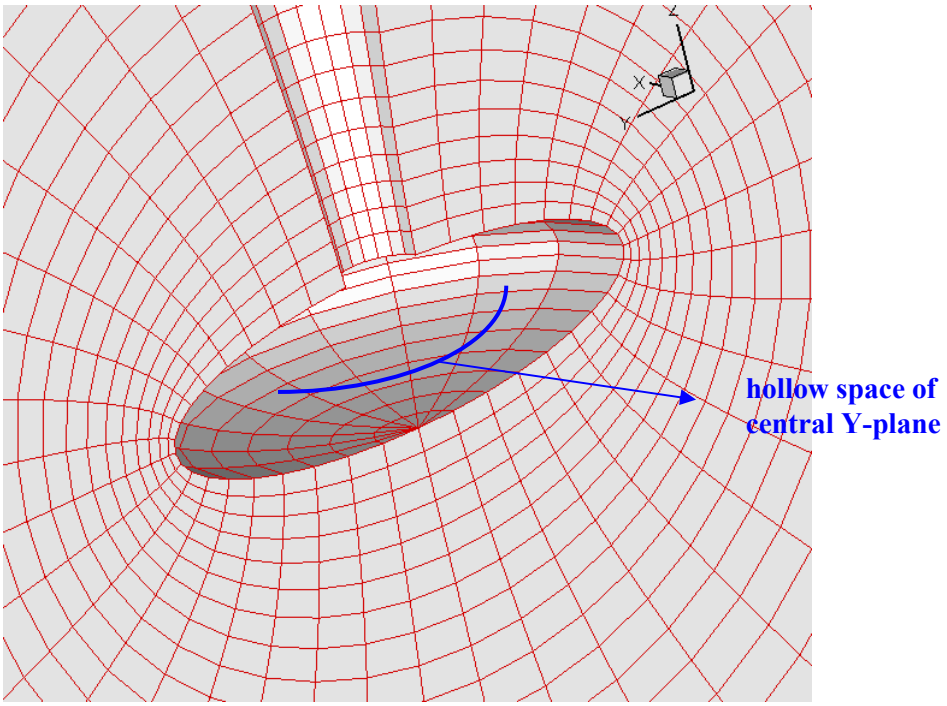


Fig. 4.8 Cross sectional zoom on the center of the mesh

We see a zoom shot of the ellipsoidal body in the center of the domain in Fig. 4.8. This figure is intended to show the perfect orthogonality of the mesh. It is clearly seen that all lines connecting the nodes of the mesh approach perpendicularly onto the surface contours of the solid ellipsoidal body of the center. We owe this feature to the orthogonality of the oblate spheroidal coordinate system.

A FORTRAN code has been developed to generate the mesh shown in Fig. 4.7 and to implement the iterative cycle of Eqn. (4.2). The code generates the 3-D mesh in desired resolution and implements the routine to obtain the solution of the potential function. This test case can be assumed to be heat-conduction problem within the volume in between inside of the outer sphere and the outside of the inner ellipsoid. The following boundary conditions were used;

Temperature on the surface of the inner ellipsoid: 30°C

Temperature on the surface of the outer sphere: 100°C

An initial guess of 40°C was assumed at all nodes except those on the contours of the boundary surfaces. A 2-D representation of the cross sectional view of the solution is graphically shown in Fig. 4.9 (a-c);

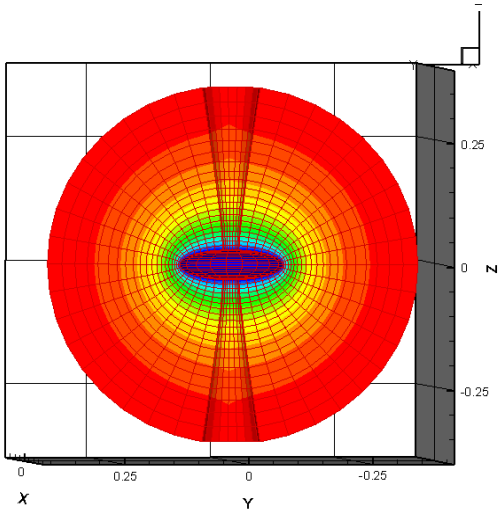


Fig. 4.9a

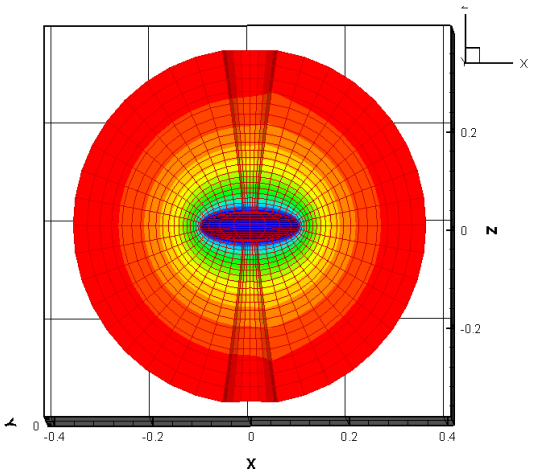


Fig. 4.9b

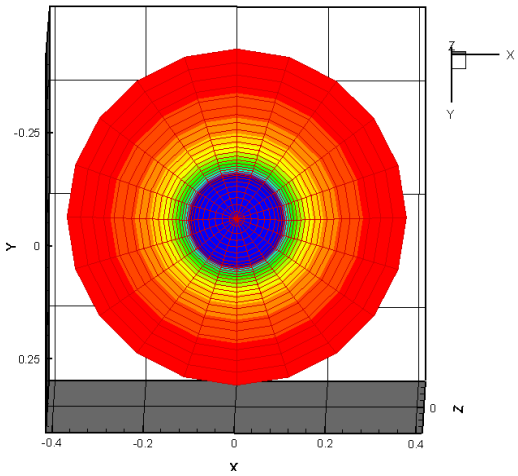


Fig. 4.9c

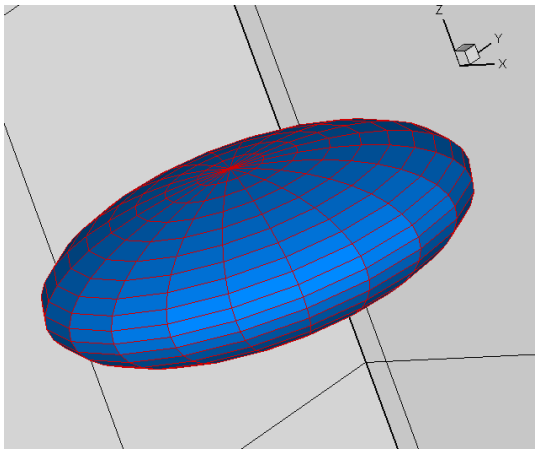


Fig. 4.10

Fig. 4.9a, 4.9b and 4.9c shows graphical representations of the solution field for 3-D temperature field, respectively at cross section around x-axis, y-axis and z-axis. The symmetry in the solution is a good indication that the FORTRAN code yielded a correct solution of Eqn. (4.2).

Fig. 4.10 shows the 3-D ellipsoid around which the solution to the potential function is sought. The surface of the outer sphere, which is assumed to be constant at T=100°C is represented with the red color in Figs. 4.9a, 4.9b and 4.9c. The surface of the inner ellipsoid, which is assumed to be constant at T=30°C is represented with the blue color. The hollow cavities in the center of the graphical representation of Figs. 4.9a, 4.9b and 4.9c represent the cold surface of the solid body of Fig. 4.10 in the center of the domain.

- **Trial with a non-symmetric 3-D Case:**

In order to test the code, the boundary conditions have been changed and a source term was added to Eqn. (4.2), after which the equation to solved turned to;

$$\psi_{i,j,k} = \frac{-1}{AP}\left[(AW)\psi_{i-1,j,k} + (AE)\psi_{i+1,j,k} + (AS)\psi_{i,j-1,k} + (AN)\psi_{i,j+1,k} + (AL)\psi_{i,j,k-1} + (AU)\psi_{i,j,k+1}\right] + SOURCE_{i,j,k} \qquad (4.3)$$

The new boundary conditions were set as follows;

Initial temperature on the surface of the inner ellipsoid: 20°C

Initial temperature on the surface of the outer sphere: 50°C

The source was set to be two distinct points at constant temperature of 50°C on the upper and lower front portions of the central ellipsoid body. The solution was obtained in the 3-D space. A two dimensional representation of the central Y plane is shown in Fig. 4.11

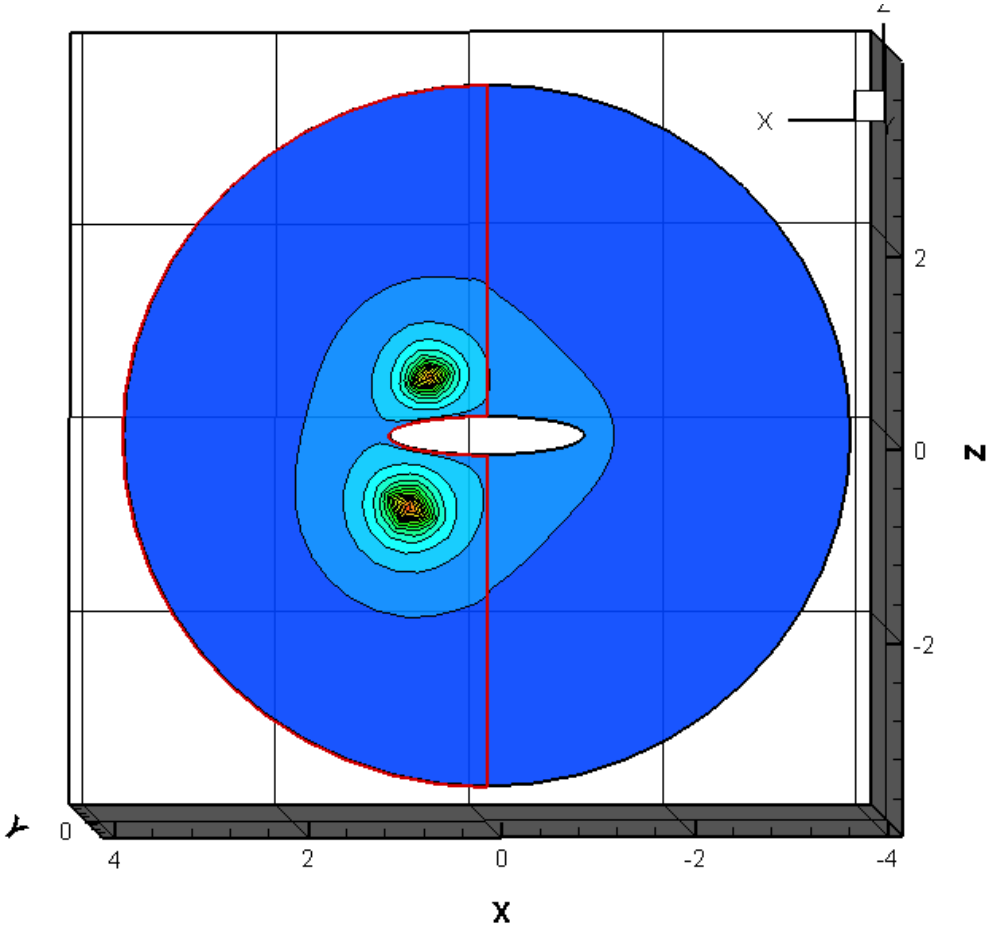


Fig. 4.11 Cross sectional view of the solution field at y=0 (side view)

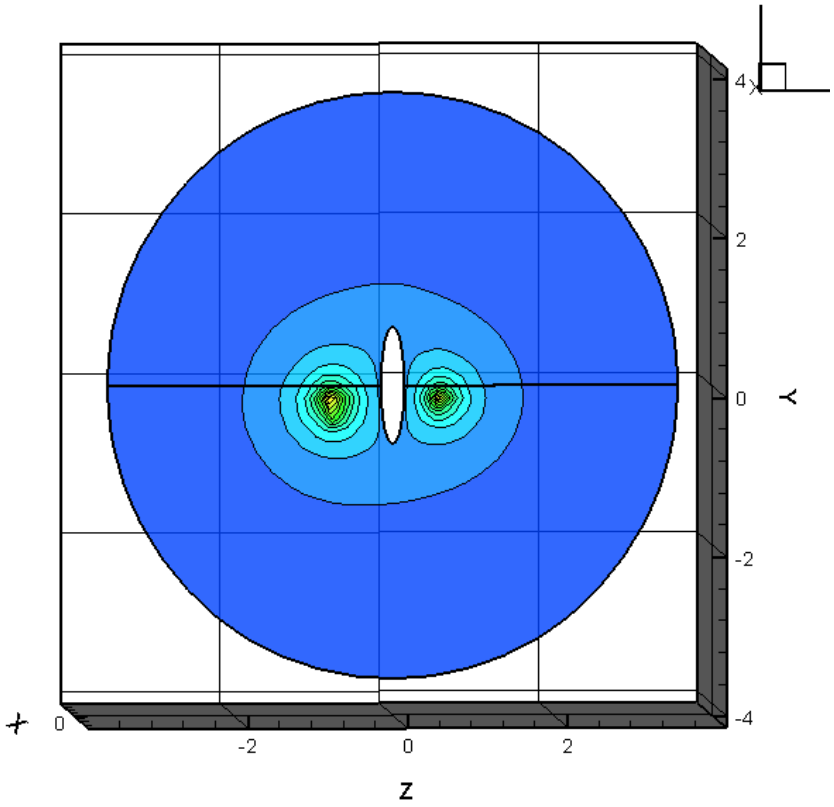


Fig. 4.12 Cross sectional view of the solution field at x=0 (upper view)

Upon examination of the temperature contours shown in Fig. 4.11 and 2.12 it is concluded that the code worked perfectly for a non-symmetric 3-D case.

4.2.1. Effects of the Selection of Oblate Spheroidal Coordinate System in the Solution Field

Unlike the spherical polar coordinate system, the oblate spheroidal coordinate system (η,θ,φ) comprises hyperbolic trigonometric functions for back conversion to Cartesian coordinates (x,y,z). Conversion from computational space to the physical space can be made according to Eqn. (3.3 – 3.5), as follows;

$$x = aCosh(\eta)Sin(\theta)Cos(\varphi) \tag{4.4}$$

$$y = aCosh(\eta)Sin(\theta)Sin(\varphi) \tag{4.5}$$

$$z = aSinh(\eta)Cos(\theta) \tag{4.6}$$

Due to the presence of “cosh” and “sinh” terms in Eqn. (4.4 – 4.6), the conversion results in a non-uniform mesh distribution in the physical space. As the “sinh” and “cosh” terms approach almost equal results when θ or η exceeds π and represent a hyperbolic curve approaching to infinity, the radial mesh spacing in the physical space exhibits exactly the same character. Even if the code developer defines constant radial mesh spacing throughout the computational domain, the conversion in the physical domain results in an extending or widening radial mesh spacing in the direction of infinity of the physical domain.

To better illustrate the effect of the coordinate system selection, we will now revert back to Fig. 4.1 showing a mesh in a spherical polar coordinate system and compare it with a mesh from an oblate spheroidal system.

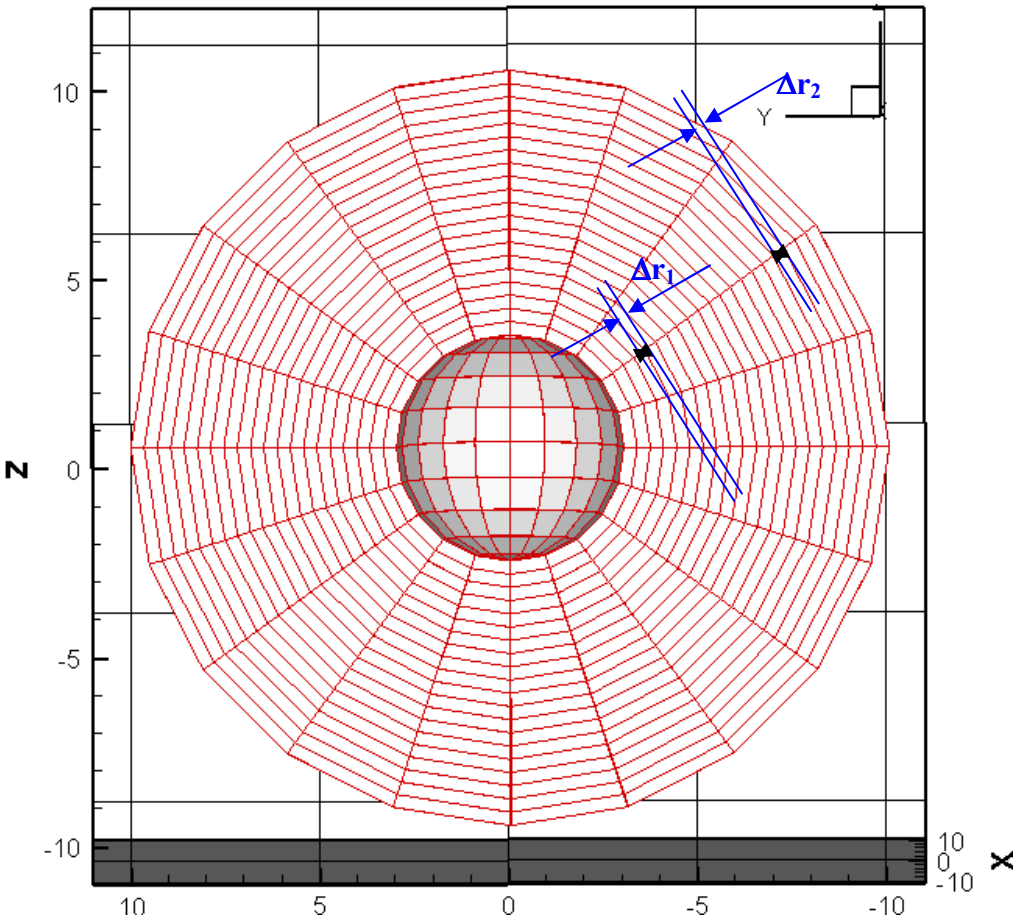


Fig. 4.13. Cross sectional view of the mesh in spherical polar coordinates

It is clear that $\Delta r_1 = \Delta r_2$ illustrated in the unclustered mesh of the spherical polar coordinates. The same holds for the computational space as well. Let us now compare this with the unclustered mesh of the oblate spheroidal coordinates (see Fig. 4.6) having exactly the same size, spacing and number of nodes.

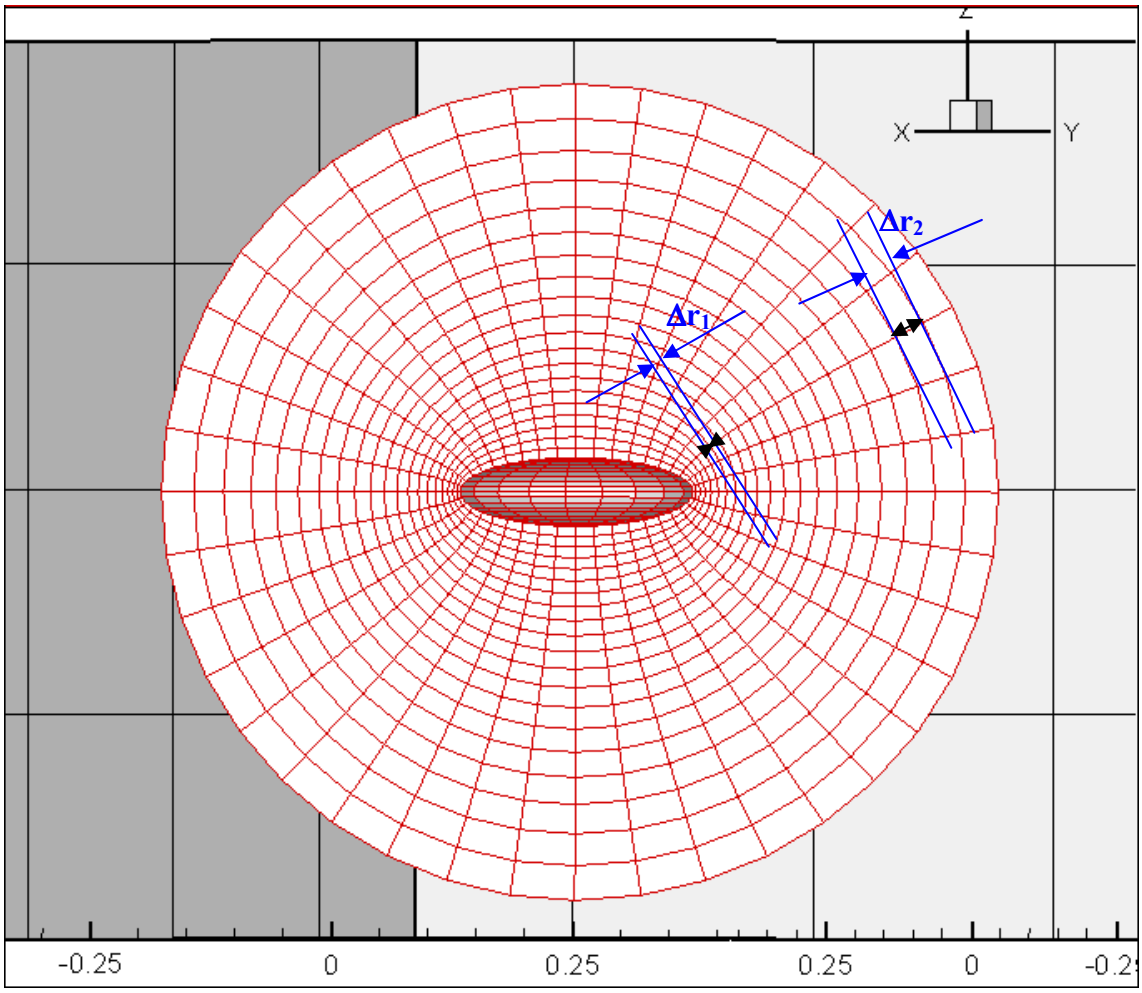


Fig. 4.14. Cross sectional view of 3-D domain comprising the 3-D ellipsoidal body

It is evident that $\Delta r_1 < \Delta r_2$ as illustrated in Fig. 4.14. We must note that the Δr is kept constant allover the computational domain and no grid clustering was adopted for the mesh of Fig. 4.14.

Briefly, the selection of the oblate spheroidal coordinates was found to be very useful for the model problem, especially in terms of the following two reasons;

1- It eliminated the need for grid clustering, and
2- It provided the opportunity to keep the radial spacing constant in the computational domain while providing a finer radial spacing towards the area of interest in the physical domain

4.2.2 Adaptation of Multi-Domain Approach

The FORTRAN code is modified to implement the solution procedure on three distinct overlapping meshes of varying resolution. The three meshes overlap onto each other partially where all three vary in radial dimension r only, and not in θ or φ.

The code generates a MESH1 which is the coarsest among the three and is the largest in terms of the 3-D volume it spans. The code later on generates a MESH2 whose radial mesh spacing in the computational domain is halved compared to that of MESH1 whereas the mesh spacing in the other two dimensions θ and φ kept constant. The code then generates a MESH3 whose radial mesh spacing is halved compared to that of MESH2 whereas the mesh spacing in the other two dimensions θ and φ were still kept equal to that of MESH1 or MESH2 in the 3-D computational domains.

It should be noted that mesh resolutions in all three meshes are equally the same, i.e. all three meshes have exactly the same number of nodes in all dimensions (r, θ, φ). Needless to say, since the mesh spacing radial dimension (r) is halved each time a new mesh generated, the new mesh covers a volume which is much smaller than the half volume of the previous mesh in the physical space and which is finer towards the 3-D ellipsoidal body in the center. Of course all these arguments are true only in the physical space and not in the computational space.

MESH1, MESH2 and MESH3 are shown, respectively in Figs. 4.15, 4.16 and 4.17 while a combination of all three will be shown in Fig. 4.18.

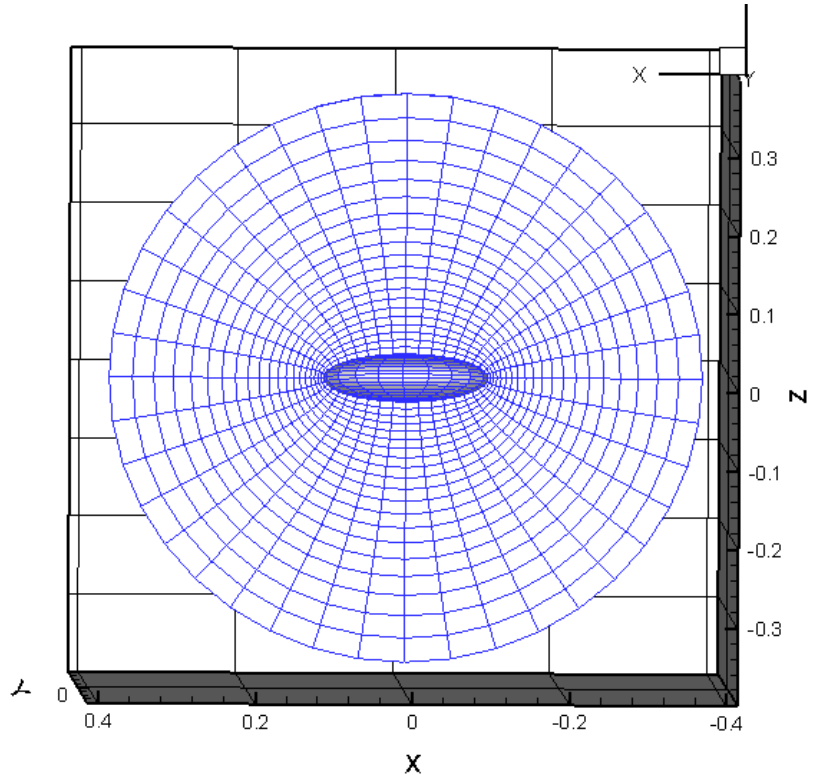


Fig. 4.15 Cross section of MESH1 (21 x 21 x 21)

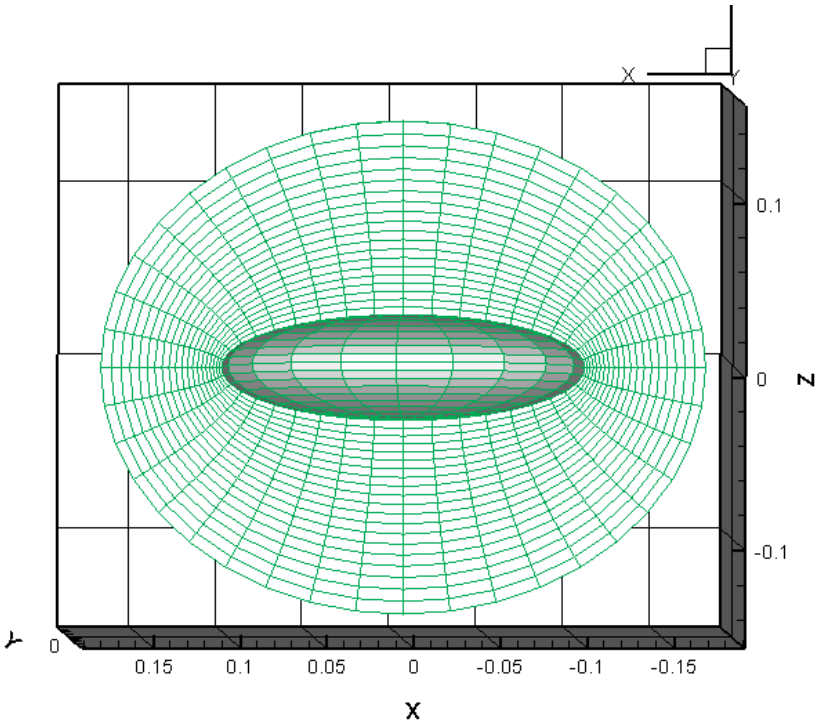


Fig. 4.16 Cross section of MESH2 (21 x 21 x 21)

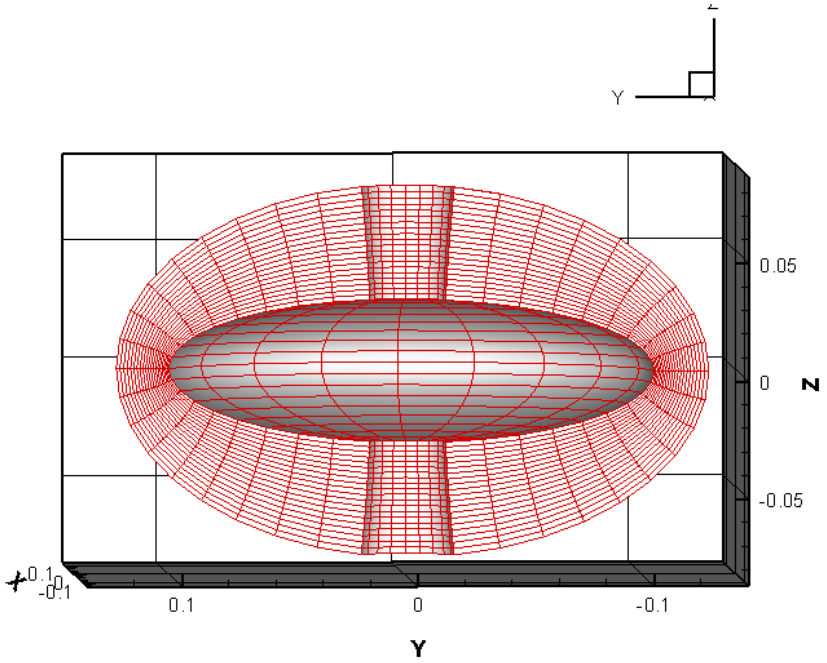


Fig. 4.17 Cross section of MESH3 (21 x 21 x 21)

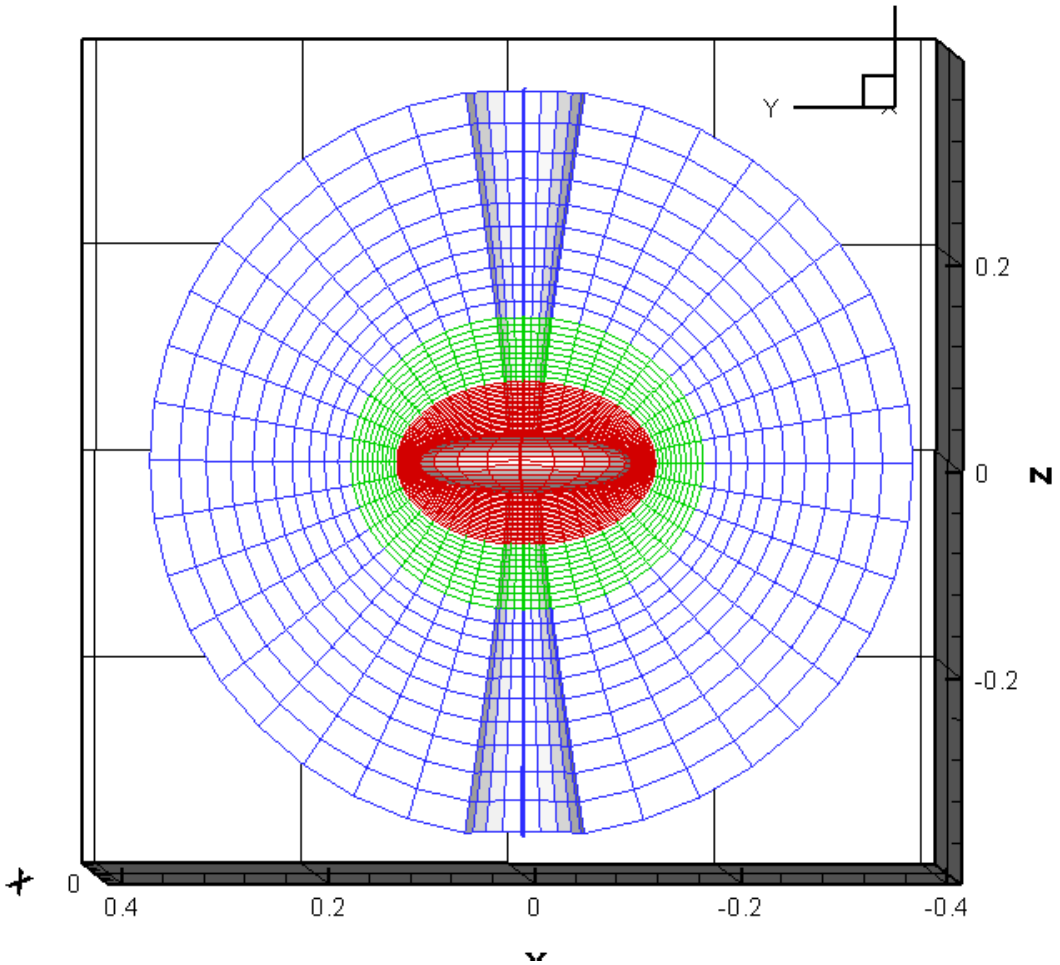


Fig. 4.18 Cross section of MESH1 + MESH2 + MESH3

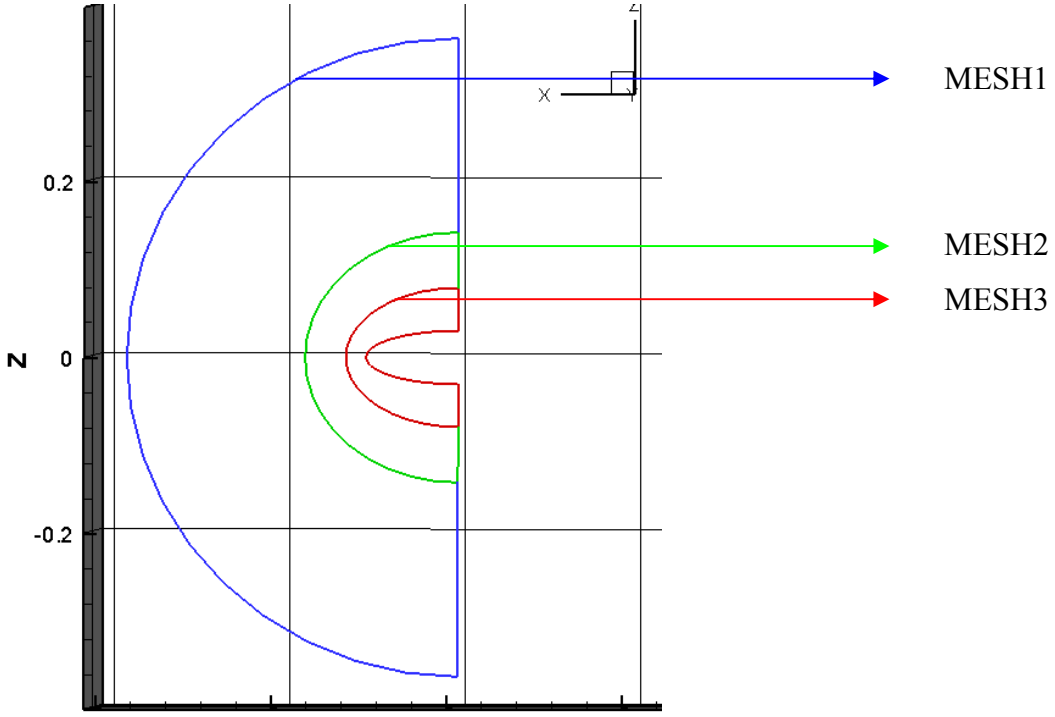
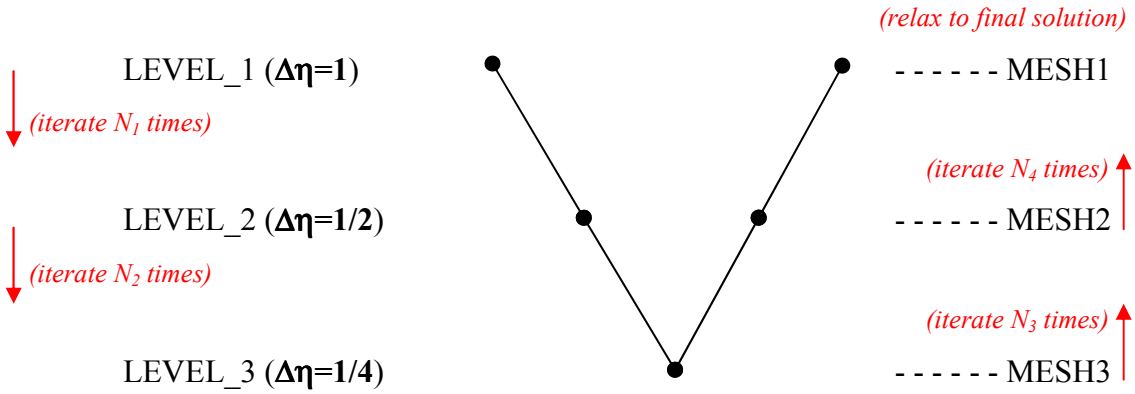


Fig. 4.19 Border lines of half of the multi-domain

The code was arranged to implement a typical V-cycle in between the meshes MESH1, MESH2 and MESH3.



While Δη was changed at each level, Δθ and Δφ were kept constant at all levels.

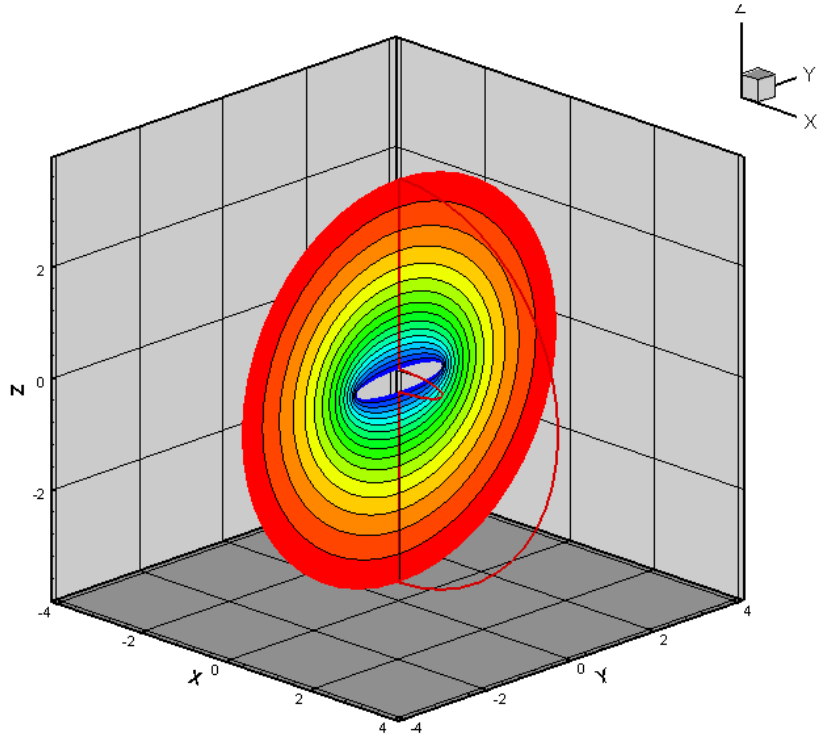


Fig. 4.20 Cross sectional view of the temperature contours obtained at the central X-plane the ellipsoid of in the multi-domain

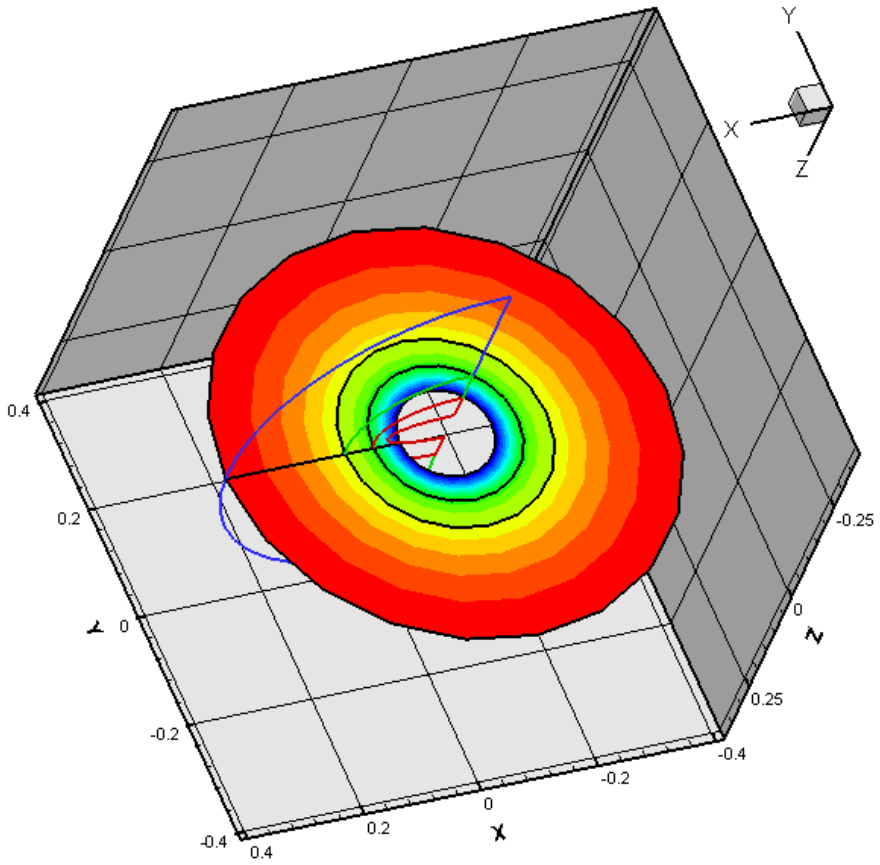


Fig. 4.21 Top view of the temperature contours of Fig.4.20

Detailed description of multi-domain/multi-grid techniques can be found at various sources in the literature, and particular in [2] and [3].

4.2.3 Effects in Response to Adaptation of Multi Domain Approach

As was mentioned in Chapter 4.3.2 above, the multi domain approach was adapted in the radial dimension η only. Hence, its effects will be investigated in terms of the number of nodes in the radial dimension and the total number of nodes in the entire domain.

Table 4.1 was prepared to show the comparison of the outcomes of the codes that adopt single domain and multi domain. All other parameters were kept constant to obtain a meaningful comparison table for understanding the effects of multi domain approach.

Table 4.1 Comparison of single/multi domains in terms of radial resolution

No. of Iteration Steps (errormax=1.E-3)	**Number of nodes**	**Single domain**	**Multi domain**	**% gain**
Nodes (11*21*21)	4.851	375	269	20,0
Nodes (17*21*21)	7.497	518	376	20,1
Nodes (21*21*21)	9.261	641	443	22,3
Nodes (27*21*21)	11.907	870	645	30,2
Nodes (35*21*21)	15.435	1.259	1090	14,7
Nodes (41*21*21)	18.081	1.579	1475	8,0

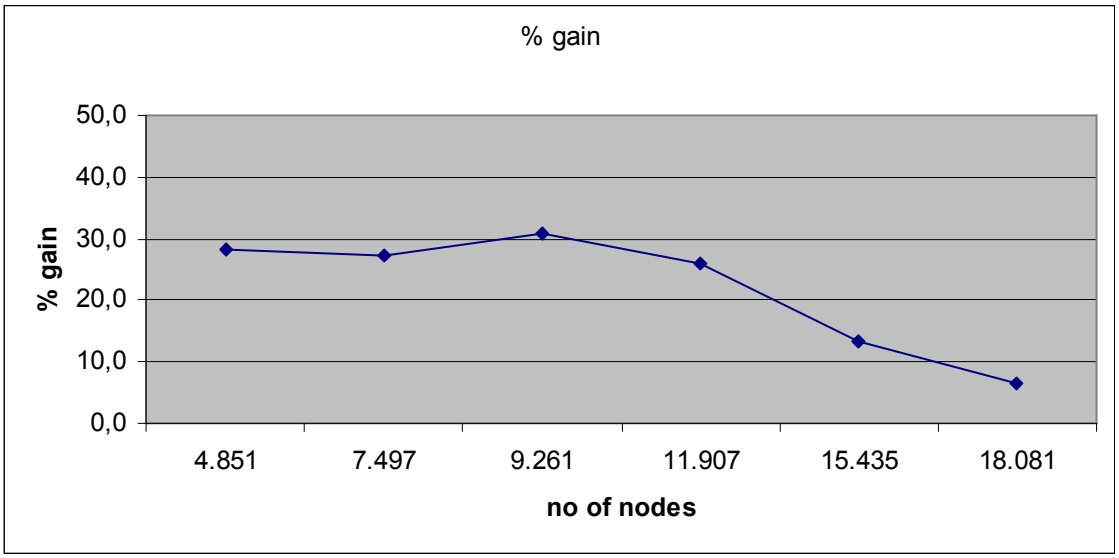


Fig. 4.22 Chart showing the gain rate in terms of the radial mesh resolution when multi domain approach is adapted

We understand from Fig. 18 that the gain rate in terms of the number of iterations the code shall implement reduces drastically as the number of nodes in the radial dimension η increases, provided that the numbers of nodes in the other two dimensions were kept constant. This might be an indication showing that the outer domain is far enough that no substantial change in the values of the potential function occurs in the far field and there is no use of employing excessive number of nodes in the radial dimension of the domain.

Table 4.2 Comparison of single/multi domains in terms of overall resolution

No. of Iteration Steps (errormax=1.E-3)	**Number Of nodes**	**Single domain**	**Multi domain**	**% gain**
Nodes (21*21*21)	9.261	641	498	22,3
Nodes (25*25*25)	15.625	923	579	37,3
Nodes (31*31*31)	29.791	1.406	978	30,4
Nodes (31*25*41)	31.775	1.537	1.065	30,7
Nodes (41*35*25)	35.875	1.898	1.588	16,3
Nodes (35*31*35)	37.975	1.713	1.274	25,6
Nodes (39*31*41)	49.569	2.068	1.619	21,7
Nodes (41*41*41)	68.921	2.467	1.888	23,5

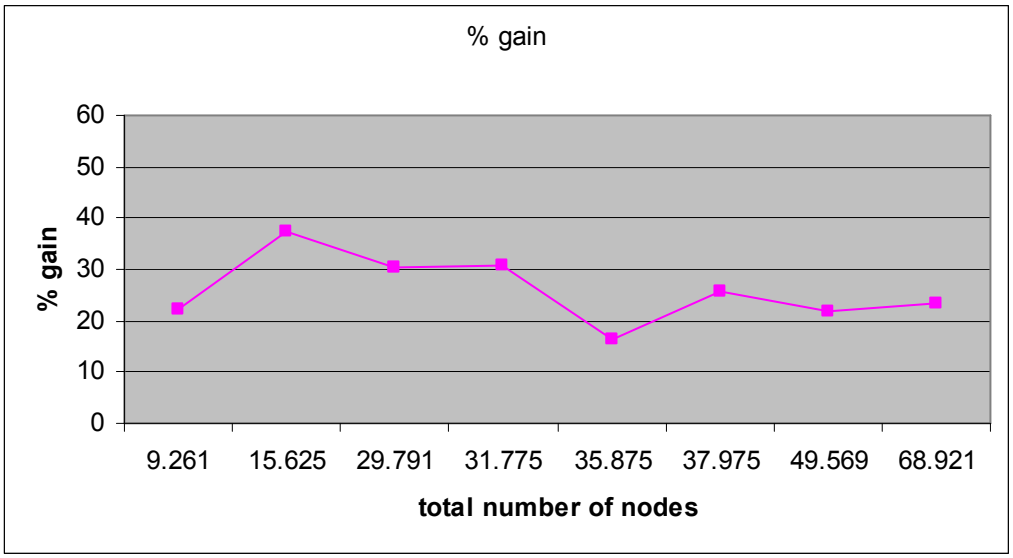


Fig.4.23 Chart showing the gain rate in terms of the overall mesh resolution when multi domain approach is adapted

Fig. 4.23 shows the graphical representation of data contained in Table 4.2, in which the effects of adapting multi domains in terms of the number of iterations are contained. The rapid decrease in the gain rate at the fifth station (no of nodes: 35875) appears to result from the rapid increase in the number of nodes of radial dimension η. This indication complies with the interpretations made for Fig. 4.22 which showed that the gain rate decreases as the number of nodes in the radial dimension increases excessively.

We can argue from Fig. 4.23 that adapting multi domain approach provides the benefit of iterating approximately 25 to 30 % less compared to single domain approach. This is mainly due the fact that larger errors are smoothed at the very beginning of the iteration cycles that take place in the coarser meshes.

- **How many iterations shall be conducted on coarse mesh(es) ?**

This is really difficult to answer as manipulating a general analytical approach to presume the ideal number of iterations on coarse meshes is almost impossible. This is dependant to the circumstances of the specific problem and can best be found by trial. The present study showed that the total number of preliminary iterations on meshes other than the final mesh shall be in the range of 10 to 20 per cent of total number of iteration cycles. In other words,

the final relaxation cycles shall constitute roughly more than 80 per cent of the total number of iteration cycles.

4.3 Solution of 3-D Potential Flow

Potential flow assumption is likely to provide allowable results in high Reynolds number flows. As an example, flow around a part of a subsonic air vehicle flying at high altitudes can be solved under the potential flow assumption. The facts that viscosity will be considerably low due to high altitude assumption and that the subsonic air vehicle is flying at high speed, will provide the flow with high Re number attribute and allows solution under the potential flow assumption. As an example, the antenna of an AWACS aircraft may be put into this classification. We will now try to obtain the solution field of a 3-D ellipsoid body under the potential flow assumption.

Let us recall the governing equation of the 3-D potential flow in oblate spheroidal coordinates;

$$\nabla^2\psi = \frac{1}{a^2\left(\cosh^2(\eta)-\sin^2(\theta)\right)}\left[\frac{\partial^2\psi}{\partial\eta^2}+Tanh(\eta)\frac{\partial\psi}{\partial\eta}+\frac{\partial^2\psi}{\partial\theta^2}+Cot(\theta)\frac{\partial\psi}{\partial\theta}\right] + \frac{1}{a^2Cosh^2(\eta)Sin^2(\theta)}\frac{\partial^2\psi}{\partial\varphi^2} \tag{4.7}$$

which takes the following form after discretization (see Chapter 3);

$$\left[\frac{Q(\eta,\theta)Sin(\theta)}{(\Delta\eta)^2}+\frac{Q(\eta,\theta)Tanh(\eta)Sin(\theta)}{2\Delta\eta}\right]\psi_{i-1,j,k}$$
$$+\left[\frac{Q(\eta,\theta)Sin(\theta)}{(\Delta\eta)^2}+\frac{Q(\eta,\theta)Tanh(\eta)Sin(\theta)}{2\Delta\eta}\right]\psi_{i+1,j,k}$$
$$+\left[\frac{Q(\eta,\theta)Sin(\theta)}{(\Delta\theta)^2}+\frac{Q(\eta,\theta)Cos(\theta)}{2\Delta\theta}\right]\psi_{i,j-1,k}$$
$$+\left[\frac{Q(\eta,\theta)Sin(\theta)}{(\Delta\theta)^2}+\frac{Q(\eta,\theta)Cos(\theta)}{2\Delta\theta}\right]\psi_{i,j+1,k}$$
$$+\left[\frac{Sin(\theta)}{(\Delta\varphi)^2}\right]\psi_{i,j,k-1}+\left[\frac{Sin(\theta)}{(\Delta\varphi)^2}\right]\psi_{i,j,k+1}$$
$$+\left[\frac{-2Q(\eta,\theta)Sin(\theta)}{(\Delta\eta)^2}+\frac{-2Q(\eta,\theta)Sin(\theta)}{(\Delta\theta)^2}+\frac{-2}{(\Delta\varphi)^2}\right]\psi_{i,j,k}=0 \qquad (4.8)$$

The definition of Q(η,θ) can be found in Chapter 3 above. We will now try to solve Eqn.(4.8) for obtaining the solution of potential flow over a 3-D ellipsoidal body. An external flow will be assumed where the outer borders of the domain is defined by a sphere which is sufficiently large and hence far from the solid body in the center. The difficulty appears to convert the model problem of heat conduction until this page into a uniform potential flow.

4.3.1. How to Model a Potential Flow

We solved the Laplace equation in previous sections and modeled the case as a heat conduction problem in three dimensions. Now, we will use exactly the same physical space and model the problem as a three dimensional flow problem. It was relatively easy when dealing with heat conduction as the boundary conditions were, likewise, relatively easy to determine. Now, we have to convert the problem and model an external flow. What we are going to solve is a potential function (ψ), where we do not know values of the potential function on either the surface of the inner ellipsoid or the outer sphere encapsulating the entire domain. Furthermore, we do not know the values of the potential function on the cutting surfaces of the latter two angular dimensions (θ and φ). Please also once again note that (θ) spans from 0 to π while (φ) spans from 0 to 2π. The great challenge begins

herewith and solved by dealing with the boundary conditions in terms of the derivatives of the potential function rather than the potential function itself. This type of boundary condition is named as *Neumann condition* [7, pp.410]

(i) Boundary Conditions on the Inner Ellipsoid

As the inner ellipsoid is assumed to be solid body through which no penetration occurs, the velocity component normal to the surface of the inner ellipsoid shall be zero. The velocity component normal to the surface of the inner ellipsoid can be expressed as the normal derivative of the potential function ψ .

$$\frac{\partial \psi}{\partial \vec{n}} = 0 \qquad (4.9)$$

In the present case, the coordinate component normal to the surface of the ellipsoid is η. Expressing the velocity component in terms of the potential function (ψ) , we obtain ;

$$\frac{\partial \psi}{\partial \eta} = 0 \qquad (4.10)$$

Upon applying forward differencing, we obtain the following discrete form for the velocity component;

$\frac{\psi_2 - \psi_1}{\Delta \eta} = 0$, and it follows that

$\psi_2 - \psi_1 = 0 \quad and\ thus,\ \psi_2 = \psi_1$

Applying this boundary condition around the entire surface of the 3-D ellipsoid, we can argue that the radial velocity component on the surface of the inner ellipsoid (i.e. at i=1) will be maintained equal to the radial velocity component on its immediate vicinity (i.e. at i=2). In result, the as *Neumann condition* is applied as follows in the code:

$$\psi_{1,j,k}\Big|_{j}^{NJ} = \psi_{2,j,k}\Big|_{j}^{NJ} \tag{4.11a}$$

$$\psi_{1,j,k}\Big|_{k}^{NK} = \psi_{2,j,k}\Big|_{k}^{NK} \tag{4.11b}$$

Please note that the potential function is designated as ψ whereas the velocity components are designated as V_η, V_θ and V_φ., the three of the latter are derivatives of the potential function with respect to the corresponding physical dimension.

(ii) Boundary Conditions on the Outer Spheroid

In order to obtain the boundary conditions to be applied on the external borders of the domain, we have to describe the velocity field in the domain. The gradient of the potential function ψ is as follows;

$$grad\,\psi = \frac{1}{a(Cosh^2\eta - Sin^2\theta)^{1/2}}\left[e_\eta \frac{\partial\psi}{\partial\eta} + e_\theta \frac{\partial\psi}{\partial\theta}\right] + e_\varphi \frac{1}{aCosh\eta Sin\theta}\frac{\partial\psi}{\partial\varphi} \tag{4.12}$$

As we are trying to obtain the solution field of an external flow, we will assume that the outer borders of the domain reflects uniform flow conditions and are sufficiently far from the inner ellipsoid to avoid interference of 3-D flow stream around the 3-D ellipsoid. In essence, the velocity component in the far field shall have only one component in the physical space, i.e. the V_∞. and no radial or angular components:

Let us now study on the radial component of the velocity in the physical space. Deducting from the gradient of the potential function, the radial component can be expressed as;

$$V_\eta = \frac{1}{a(Cosh^2\eta - Sin^2\theta)^{1/2}}\frac{\partial\psi}{\partial\eta}\vec{e}_\eta \tag{4.13}$$

Recalling that we assumed uniform flow V_∞ on the outer borders of the domain, we can argue that there shall be no radial component of the velocity field on the far field, or

namely the outer sphere. Let us now try to express the radial component of the velocity in terms of the uniform flow field.

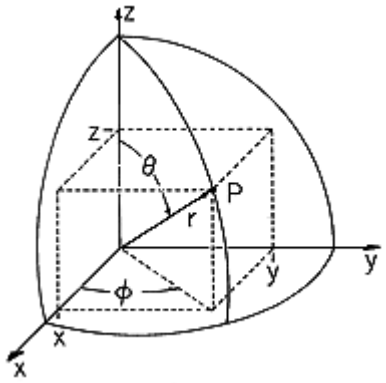


Fig. 4.24a

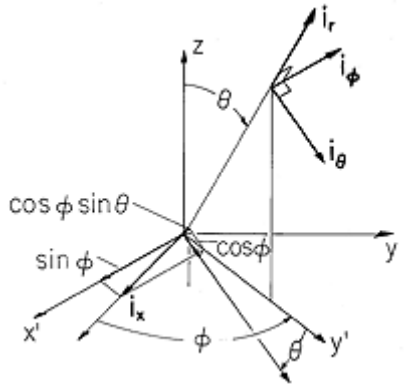


Fig. 4.24b

Figs. 4.24a and 4.24b are given to illustrate the vector transformation from spherical coordinates (r,θ,ϕ) to Cartesian coordinates. Adopting our designation in oblate spheroidal coordinates (η,θ,φ), we can deduce that the trigonometric relation in between V_∞ and V_η can be expressed as follows;

$$V_\eta = -V_\infty Sin(\theta)Cos(\varphi) \tag{4.14}$$

Equating the latter two equations (4.13) and (4.14), we can now write;

$$\frac{1}{a(Cosh^2\eta - Sin^2\theta)^{1/2}}\frac{\partial \psi}{\partial \eta} = -V_\infty Sin(\theta)Cos(\varphi) \tag{4.15}$$

Let us now discretize Eqn.(4.15) using a first order backward differencing ;

$$\frac{1}{a(Cosh^2\eta - Sin^2\theta)^{1/2}}\frac{\psi_{NX} - \psi_{NX-1}}{\Delta \eta} = -V_\infty Sin(\theta)Cos(\varphi) \tag{4.16}$$

Rewriting Eqn. (4.16) we obtain the following expression for the potential function on the outer borders of the domain;

$$\psi_{NX} = \psi_{NX-1} - V_{\infty} Sin(\theta) Cos(\varphi) \bullet a(Cosh^2\eta - Sin^2\theta)^{1/2} \Delta\eta \tag{4.17}$$

Assigning a dummy function, RES(η,θ,φ)

$$RES = V_{\infty} Sin(\theta) Cos(\varphi) \bullet a\Delta\eta\sqrt{(Cosh^2\eta - Sin^2\theta)} \tag{4.18}$$

the *Neumann boundary conditions* on the outer borders of the domain takes the following form in the code;

$$\psi_{NX,j,k}\Big|_j^{NJ} = \psi_{NX-1,j,k}\Big|_j^{NJ} - RES_{NX,j,k}\Big|_j^{NJ} \tag{4.19a}$$

$$\psi_{NX,j,k}\Big|_k^{NK} = \psi_{NX-1,j,k}\Big|_k^{NK} - RES_{NX,j,k}\Big|_k^{NK} \tag{4.19b}$$

Unlike all previous cases of heat conduction problems, the boundary conditions in this section are subject to change as the solution proceeds and are therefore called kinematic boundary conditions.

4.3.2. Velocity Components in Oblate Spheroidal Coordinates and Back Transformation into Physical Space

In order to determine the velocity components in the oblate spheroidal coordinates and transform these into the Cartesian space, we will revert back to the gradient of the potential function ψ;

$$grad\,\psi = \frac{1}{a(Cosh^2\eta - Sin^2\theta)^{1/2}}\left[e_{\eta}\frac{\partial\psi}{\partial\eta} + e_{\theta}\frac{\partial\psi}{\partial\theta}\right] + e_{\varphi}\frac{1}{aCosh\eta Sin\theta}\frac{\partial\psi}{\partial\varphi} \tag{4.20}$$

Separating Eqn.(4.20) into parts, we obtain ;

$$V_\eta = \frac{1}{a(Cosh^2\eta - Sin^2\theta)^{1/2}} \frac{\partial \psi}{\partial \eta} \tag{4.21}$$

$$V_\theta = \frac{1}{a(Cosh^2\eta - Sin^2\theta)^{1/2}} \frac{\partial \psi}{\partial \theta} \tag{4.22}$$

$$V_\varphi = \frac{1}{aCosh\eta Sin\theta} \frac{\partial \psi}{\partial \varphi} \tag{4.23}$$

Now we will discretize Eqns. (4.21) (4.22) and (4.23) using first order central differencing in order to obtain velocity components in the computational domain.

$$V_\eta = \frac{1}{a(Cosh^2\eta - Sin^2\theta)^{1/2}} \left(\frac{\psi_{i+1,j,k} - \psi_{i-1,j,k}}{2\Delta\eta}\right) \tag{4.24}$$

$$V_\theta = \frac{1}{a(Cosh^2\eta - Sin^2\theta)^{1/2}} \left(\frac{\psi_{i,j+1,k} - \psi_{i,j-1,k}}{2\Delta\theta}\right) \tag{4.25}$$

$$V_\varphi = \frac{1}{aCosh\eta Sin\theta} \left(\frac{\psi_{i,j,k+1} - \psi_{i,j,k-1}}{2\Delta\varphi}\right) \tag{4.26}$$

It should be noted velocity components shall be discretized using backward or forward differencing schemes when necessary e.g. around boundaries.

Having obtained algebraic expressions for the velocity components, we have to determine corresponding velocity components in the Cartesian space. The vector transformation can be derived from Eqn. (3.3), (3.4) and (3.5) as follows;

$$x = aCosh(\eta)Sin(\theta)Cos(\varphi) \tag{4.27}$$

$$y = aCosh(\eta)Sin(\theta)Sin(\varphi) \tag{4.28}$$

$$z = aSinh(\eta)Cos(\theta) \tag{4.29}$$

We will now take derivatives of Eqns. (4.27) to (4.29) with respect to time;

$$\frac{dx}{dt} = \frac{\partial x}{\partial \eta}\frac{d\eta}{dt} + \frac{\partial x}{\partial \theta}\frac{d\theta}{dt} + \frac{\partial x}{\partial \varphi}\frac{d\varphi}{dt} \tag{4.30}$$

$$\frac{dy}{dt} = \frac{\partial y}{\partial \eta}\frac{d\eta}{dt} + \frac{\partial y}{\partial \theta}\frac{d\theta}{dt} + \frac{\partial y}{\partial \varphi}\frac{d\varphi}{dt} \tag{4.31}$$

$$\frac{dz}{dt} = \frac{\partial z}{\partial \eta}\frac{d\eta}{dt} + \frac{\partial z}{\partial \theta}\frac{d\theta}{dt} + \frac{\partial z}{\partial \varphi}\frac{d\varphi}{dt} \tag{4.32}$$

Having mentioning that

$$V_\eta = \frac{d\eta}{dt} \qquad V_\theta = \frac{d\theta}{dt} \qquad V_\varphi = \frac{d\varphi}{dt}$$

let us now find the partial derivatives using Eqns. (4.27) to (4.29) with respect to the ordinates of the computational domain;

$$\frac{\partial x}{\partial \eta} = aSinh(\eta)Sin(\theta)Cos(\varphi) \tag{4.33a}$$

$$\frac{\partial x}{\partial \theta} = aCosh(\eta)Cos(\theta)Cos(\varphi) \tag{4.33b}$$

$$\frac{\partial x}{\partial \varphi} = -aCosh(\eta)Sin(\theta)Sin(\varphi) \tag{4.33c}$$

$$\frac{\partial y}{\partial \eta} = aSinh(\eta)Sin(\theta)Sin(\varphi) \tag{4.34a}$$

$$\frac{\partial y}{\partial \theta} = aCosh(\eta)Cos(\theta)Sin(\varphi) \tag{4.34b}$$

$$\frac{\partial y}{\partial \varphi} = aCosh(\eta)Sin(\theta)Cos(\varphi) \tag{4.34c}$$

$$\frac{\partial z}{\partial \eta} = aCosh(\eta)Cos(\theta) \tag{4.35a}$$

$$\frac{\partial z}{\partial \theta} = -aSinh(\eta)Sin(\theta) \tag{4.35b}$$

$$\frac{\partial z}{\partial \varphi} = 0 \tag{4.35c}$$

Now, inserting these partial derivatives into Eqns. (4.30) to (4.32), we obtain the velocity components in the Cartesian space;

$$\frac{dx}{dt} = V_x = aSinh(\eta)Sin(\theta)Cos(\varphi)V_\eta + aCosh(\eta)Cos(\theta)Cos(\varphi)\ V_\theta$$
$$-aCosh(\eta)Sin(\theta)Sin(\varphi)\ V_\varphi \qquad (4.36)$$

$$\frac{dy}{dt} = V_y = aSinh(\eta)Sin(\theta)Sin(\varphi)V_\eta + aCosh(\eta)Cos(\theta)Sin(\varphi)\ V_\theta$$
$$+aCosh(\eta)Sin(\theta)Cos(\varphi)\ V_\varphi \qquad (4.37)$$

$$\frac{dz}{dt} = V_z = aCosh(\eta)Cos(\theta)\ V_\eta - aSinh(\eta)Sin(\theta)\ V_\theta \qquad (4.38)$$

Eqns. (4.36), (4.37) and (4.38) can now be used to back transform the velocity outcome from the code. Having found the velocity vectors in the physical domain, we can now calculate the scalar quantity of velocity using Eqn. (4.39);

$$\left|\vec{V}\right| = \sqrt{V_\eta^2 + V_\theta^2 + V_\varphi^2} \qquad (4.39)$$

4.3.3 Flow Field

A FORTRAN code is used to calculate the 3-D flow field around the ellipsoid solid body. The code solves the potential function in the volume between the outer sphere resembling the far field and the inner ellipsoid. Once the potential function is obtained throughout the region, the velocity field is calculated using Eqns. (4.24) to (4.26) and -in the physical domain- Eqns. (4.36) to (4.38).

A cross sectional view of the solutions field is shown is Fig. 4.25 .

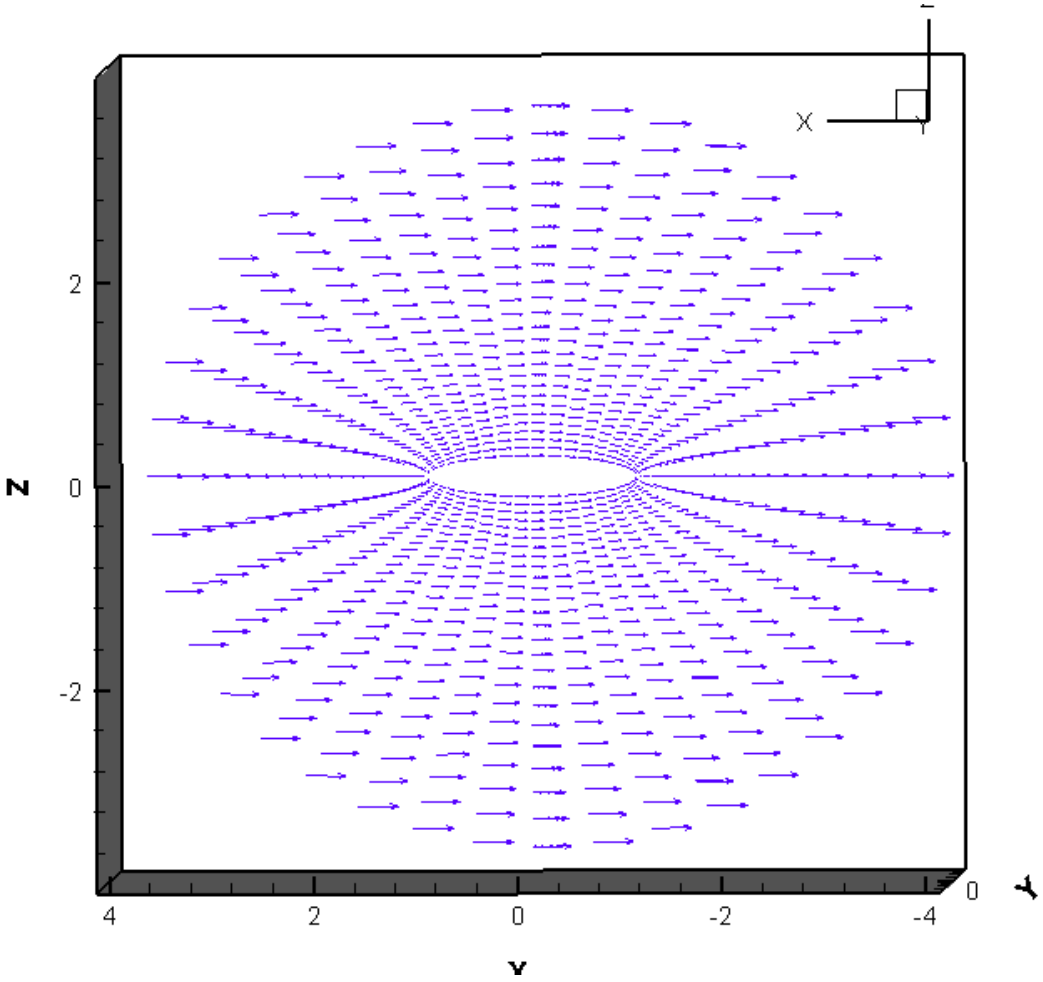


Fig. 4.25 Cross sectional side view of velocity field around the 3-D ellipsoid

We understand from the velocity field of Fig. 4.25, which is a 2-D representation of the domain cut exactly from the central Y-plane, that the code maintains uniform flow in the far fields, i.e. at regions close to the outer sphere. The flow leaves the domain at the right hand side of the figure where the flow can again be considered as a uniform flow with x-component only.

The flow also perfectly flows parallel to the surface of the inner ellipsoid on the interior and there is no penetration in the ellipsoid. We will now see a zoom shot of the velocity vectors immediately on the 1st and 2nd halves of the inner ellipsoid in, respectively, Figures 4.26a and 4.26b.

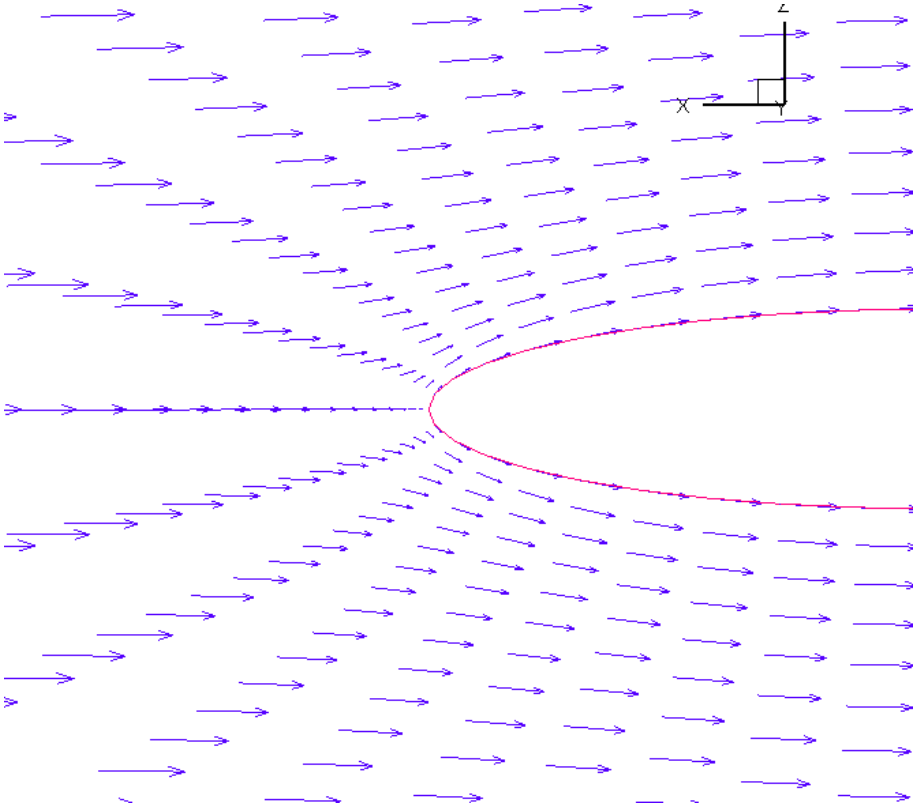


Fig. 4.26a Zoom shot of Fig. 4.25 on the leading part of the ellipsoid body

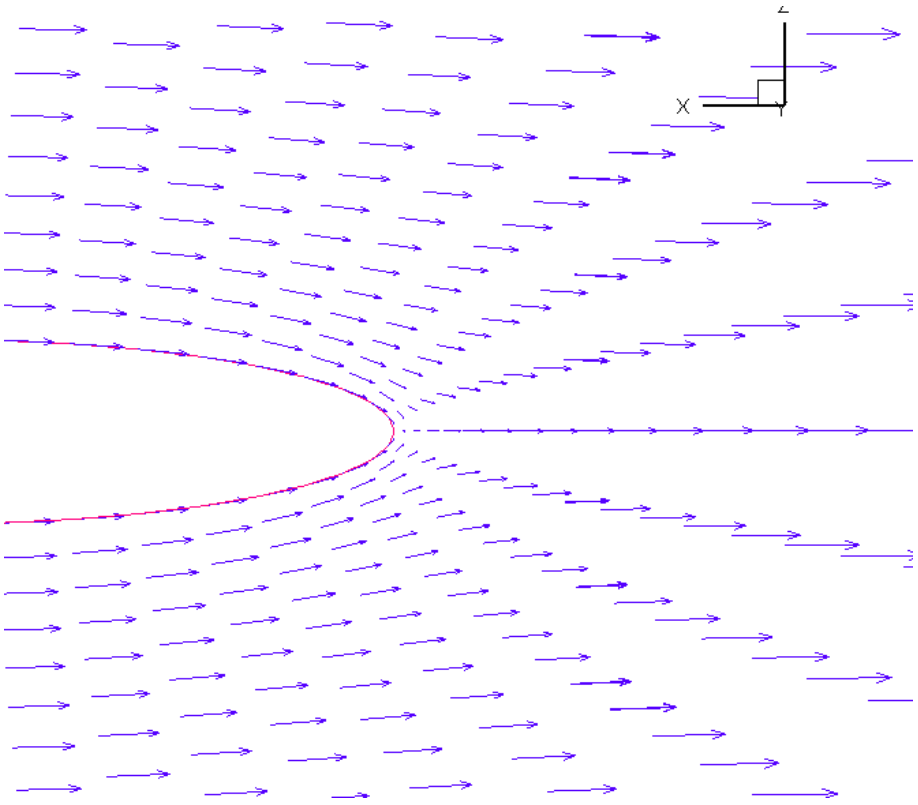


Fig. 4.26b Zoom shot of Fig. 4.25 on the trailing part of the ellipsoid body

- **Comparison With Analytical Results**

Viana et. Al [9] obtained the solution field for an irrotational, inviscid flow as shown in Fig. 4.25 in which a two dimensional representation of the flow field at the centerline of a tri-axial ellipsoid is graphically shown.

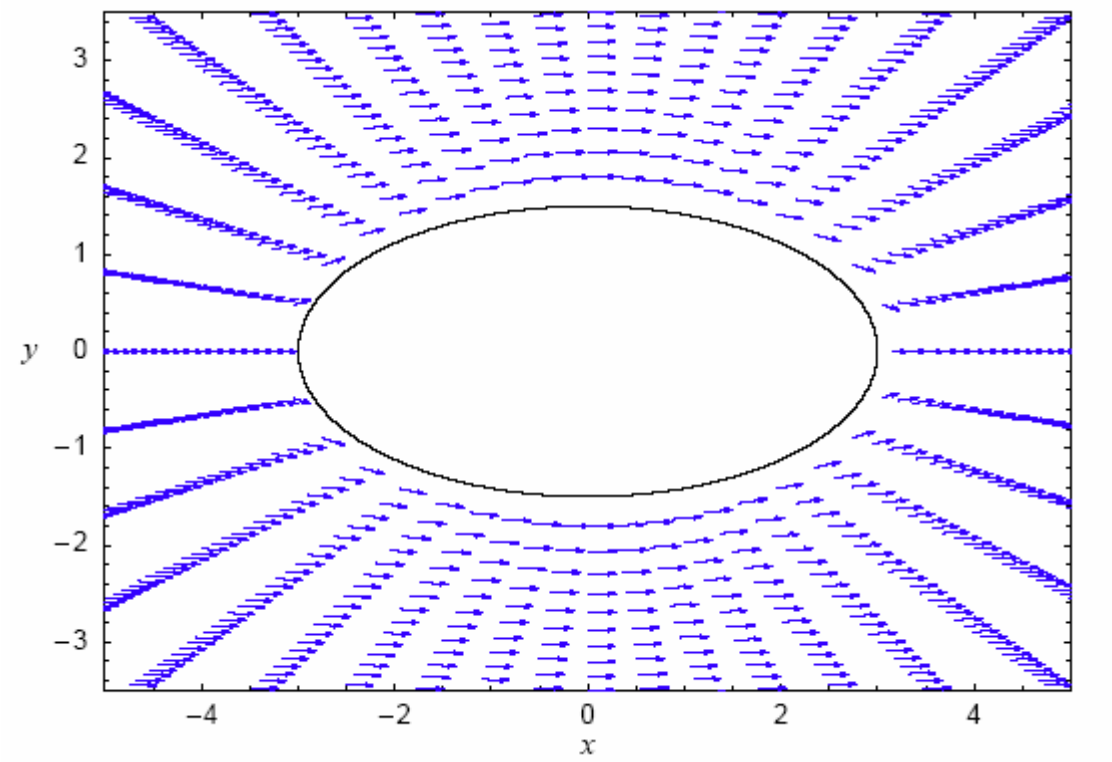


Fig. 4.27. Two dimensional representation of the velocity field at the centerline of the ellipsoid (z = 0) according to Viana et al. [9]

Let us now investigate the solution field in more detail and look at the solution field from an alternate axis.

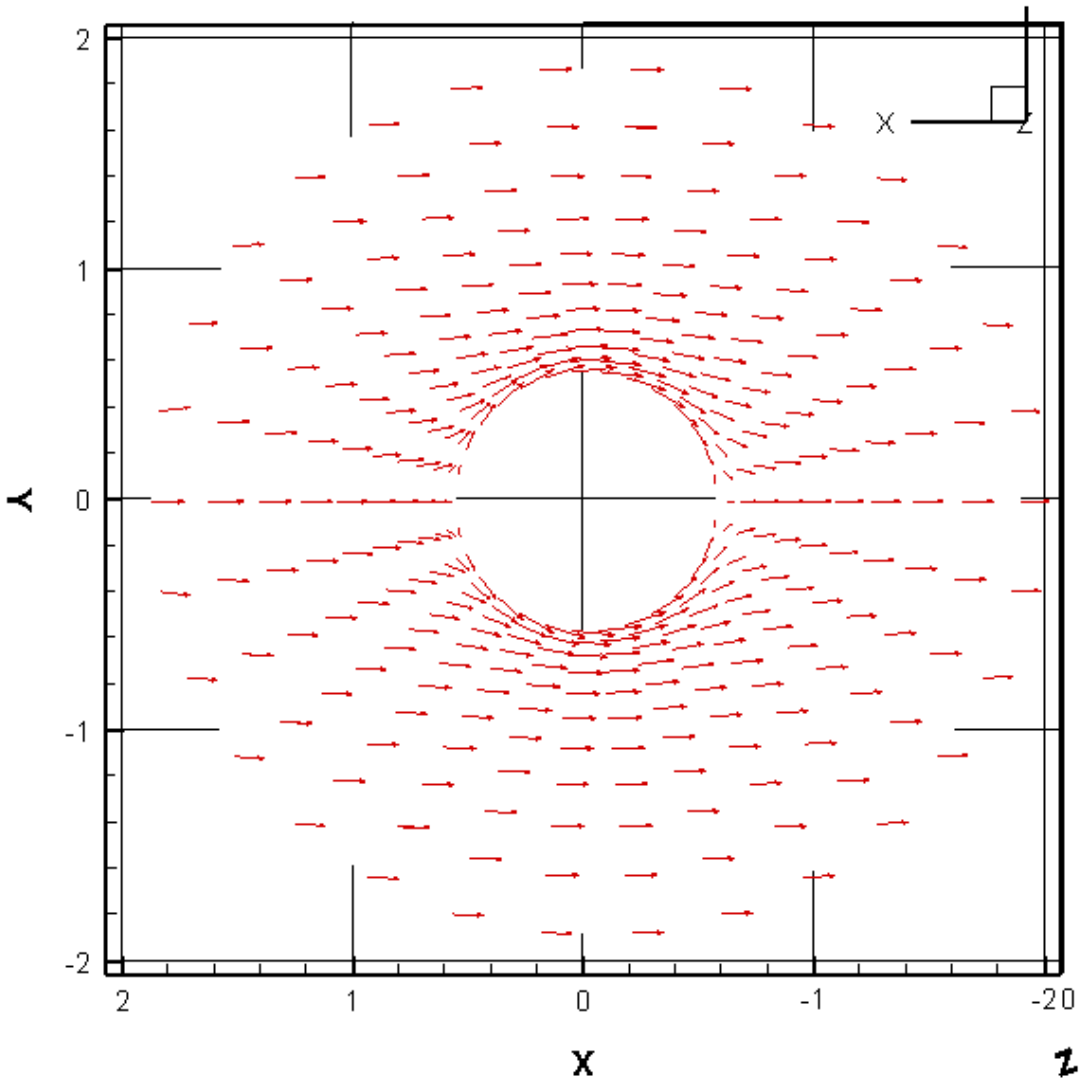


Fig. 4.28 Cross sectional view of velocity field around the 3-D ellipsoid (top view)

Fig. 4.28 is a 2-D representation of the domain cut exactly from the central Z-plane and hence is a top view of the velocity vectors found on exactly around the semi-axis of the ellipsoid body on the center of the domain. In compliance with the outcome of the previous Fig.25, the code maintains uniform flow in all far fields, the entrance on the left part and the exit region on the right part. The flow is totally parallel to the surface of the inner ellipsoid on the interior.

We will now investigate the potential field within the 3-D domain. For this purpose, we will cut a quarter of the outer sphere and see cross sections of semi Z-plane and semi Y-plane.

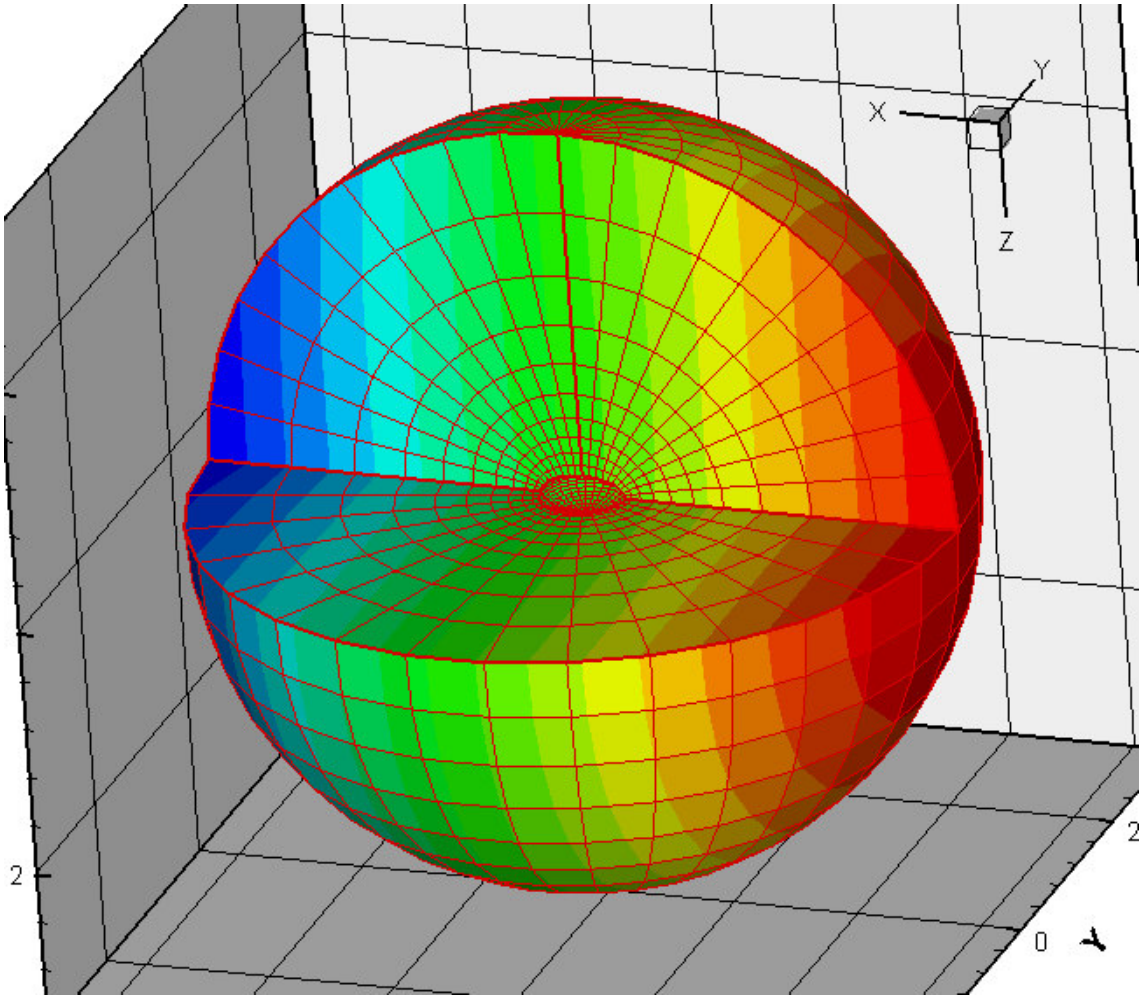


Fig. 4.29 Double cross sectional perspective view of potential field around 3-D ellipsoid

Regions shown in red color represents high potential values while regions having lower potential values are represented with, respectively, orange, yellow, blue and dark blue depending on how low the potential value at that cross section is. Recalling that the uniform flow is parallel to the x-axis, we can argue from Fig. 4.29 that color distribution along the x-axis perfectly reflects the expected potential field. The expected change in the values of the potential field is that the potential function decreases gradually in the direction of the flow.

Let us now look at the potential contours at central Z-plane and Y-plane in the solution field to see if the potential function has a proper distribution.

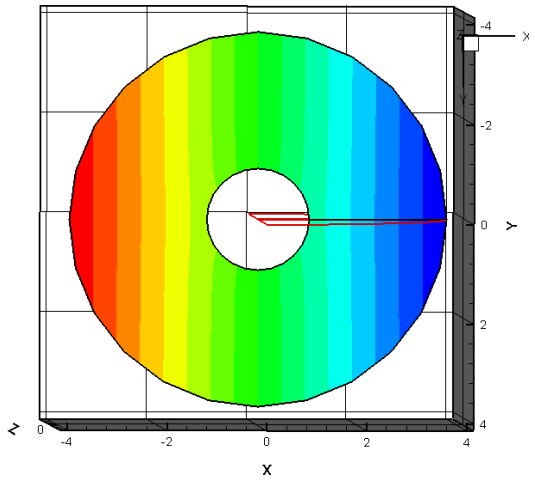


Fig. 4.30a Contours of potential function along central Z-plane

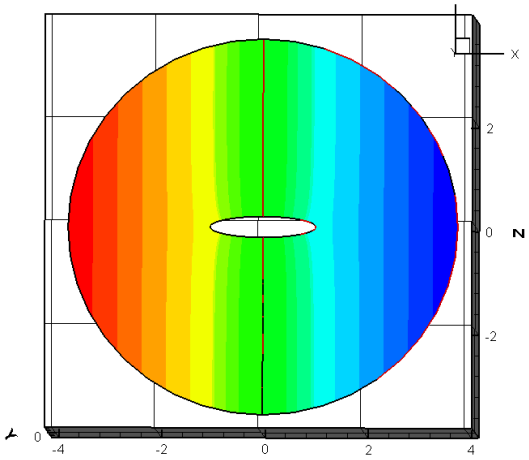


Fig. 4.30b Contours of potential function along central Y-plane

It is readily seen that the distribution of the potential function is even and decreases gradually with no irregularity. Hence, the 3-D solution field generated by the code is assumed to be correct and in compliance with the analytical results of Viana et al [9].

5. CONCLUSIONS

Having applied the mathematical modeling in either the spherical polar coordinates or in the oblate spheroidal coordinates, the FORTRAN code produced perfectly orthogonal meshes. While the computational domain of the finite difference scheme is always in the shape of a rectangular prism, the physical domain takes the form of ellipsoids or spheres or both. The 3-D meshes obtained in the volume between the ellipsoids and spheres have been found to be easy to generate and problem-free in terms of orthogonality.

Selection of oblate spheroidal coordinates has been found to comprise further advantages in all model problems of the present study. Due to the presence of hyperbolic trigonometric functions “cosh” and “sinh” in the conversion formulae of the coordinate system, the back conversion to Cartesian coordinates results in a non-uniform mesh distribution in the physical space. The fact that the “sinh” and “cosh” terms result almost equal values when θ or η exceeds π and represent a hyperbolic curve approaching to infinity, the radial mesh spacing in the physical space presents an advantageous result. While taking advance of simple coding by way of defining constant radial mesh spacing in the computational domain, an increasingly extending radial mesh spacing was obtained upon the conversion to the physical space. This is especially very advantageous in cases where an external flow is investigated and mesh spacing in far fields is much less important than mesh spacing in the center of the domain.

In brief words, the selection of oblate spheroidal coordinate system provided the following advantages towards solution.

- It eliminated the need for grid clustering
- It provided the opportunity to keep the radial spacing constant in the computational domain while providing a finer radial spacing towards the area of interest in the physical domain, thereby avoided the burden of excessive computational work for accurate results.

Applying a multi-domain approach was found to be advantageous in essence of decreasing the computational work. Since all domains of the present study are three dimensional, excessive computational work shall be expected due to large number of nodes in the domain as well as complexity of the governing equations. Having applied three levels of overlapping domains, the study showed that the computational work could be reduced approximately by 30% when compared to the computational work of conventional single domain approach.

The examples of the present study also revealed that only a few number of iterations in the coarse meshes is enough to eliminate larger errors and, later, to converge in the finest mesh. Interestingly, insisting on more iteration cycles in coarse meshes do not contribute to the benefits of the multi domain approach. In the contrary, computational work increases if the programmer adopts more iteration cycles than he shall in the coarse meshes and the approach becomes less beneficial. There is, however, no exact or easy way of determining the ideal number of iteration cycles to adopt in the coarse mesh cases or when to switch to finer meshes. The present study showed that the number of final relaxation steps shall constitute at least 80 per cent of the total number of iteration cycles.

The oblate spheroidal coordinate system was found to be appropriate for the model problem, i.e. an external flow over a 3-D ellipsoidal body. The potential flow assumption could be implemented without major problems using finite difference approximations. More conveniently, the hyperbolic nature of the coordinate transformation functions allowed solution of far fields of the external flow with relatively less computational work. Advantageously, in all cases where the area of interest is located in the center of the domain, the three dimensional meshes automatically becomes finer at the area or volume of interest.

REFERENCES

1. Hoffmann, K.A., "*Computational Fluid Dynamics For Engineers*" Engineering Education System, 1989.

2. Trottenberg, U., C. Oosterlee and A. Schüller, "*Multigrid*" Academic Press, 2001.

3. Briggs, L.W., "*A Multigrid Tutorial*", Society for Industrial and Applied Mathematics, Philadelphia PA, 1987.

4. Panton, R. L., "*Incompressible flow*", John Wiley & Sons, pp. 742-746 appendix B, 1984.

5. Moon, P. and D.E. Spencer, "*Field Theory Handbook: Including Coordinate Systems, Differential Equations and Their Solutions*" New York: Springer-Verlag, pp. 1-48, 1988.

6. Yaldizli, M. "*Multiple-Domain Analysis of Unsteady Combustion with Detailed Chemistry for a Spherical Fuel Source*" M.Sc. Thesis Boğaziçi University, 2005.

7. Blazek, J. "*Computational Fluid Dynamics, Principles and Applications*" Elsevier, 2001.

8. Marleau, L. "*Mécanique classique*" Scientific WorkPlace, Univérsite Laval, Québec Canada, 1998.

9. Viana F., T. Funada , D.D. Joseph, N. Tashiro and Y. Sonoda, "Potential flow of a second-order fluid over a tri-axial ellipsoid" *Jour. Applied Mech*. Vol. 335, January 2005.

10. Burstein, E.I. "*One of the Solutions for The Laplace Equation and Its Physical Interpretation*" Celestial Mechanics 11, pp. 79-94, 1975.

11. Haus, A. H. and Melcher, R. J., "*Vector Operations"*, http://web.mit.edu/6.013_book/www/appendices/app1.html , 1998.

12. Lomax, H., T.H. Pulliam and D.W. Zingg, "*Fundamentals of Computational Fluid Dynamics*" NASA Ames Research Center, 1999.